

# A comparison of self- and semi-supervised pretraining approaches for risk prediction from chest radiograph images

Yanru Chen<sup>1,2</sup>

YC4037@COLUMBIA.EDU

Michael T Lu<sup>1</sup>

MLU@MGH.HARVARD.EDU

Vineet K Raghu<sup>1</sup>

VRAGHU@MGH.HARVARD.EDU

<sup>1</sup> *Cardiovascular Imaging Research Center, Massachusetts General Hospital & Harvard Medical School*

<sup>2</sup> *Department of Computer Science, Columbia University*

## Abstract

Deep learning is the state-of-the-art for medical imaging tasks, but requires large, labeled datasets. For risk prediction (e.g., predicting risk of future cancer), large datasets are rare since they require both imaging and long-term follow-up. However, the release of publicly available imaging data with diagnostic labels presents an opportunity for self and semi-supervised approaches to use diagnostic labels to improve label efficiency for risk prediction. Though several studies have compared self-supervised approaches in natural image classification, object detection, and medical image interpretation, there is limited data on which approaches learn robust representations for risk prediction. We present a comparison of semi- and self-supervised learning to predict mortality risk using chest x-ray images. We find that a semi-supervised autoencoder outperforms contrastive and transfer learning in internal and external validation data.

**Keywords:** Deep learning, risk prediction, chest radiographs, self-supervised pretraining

## 1. Introduction

Deep learning [5,24] is the state of the art for medical image segmentation [18] and interpretation [17] tasks ; however, deep learning requires large, labeled datasets, which are rare. One solution is transfer learning, where models are initially trained to classify objects in large natural image data (e.g., ImageNet [11]), and then fine-tuned for the target task. However, ImageNet-based transfer learning may provide limited benefit beyond training models entirely from scratch [30]. In contrast, self-supervised techniques use unlabeled medical images to learn compressed, expressive representations. Due to the feasibility of releasing unlabeled image data, this strategy is promising for medical image analysis [34].

Beyond image interpretation, deep learning can estimate future disease risk [25,28,33,26,31] using datasets with imaging and follow-up. These tasks differ from common pretraining tasks (e.g., object detection, segmentation, etc.) in that there is not necessarily a localizable pathology (object of interest) on the image. For example, frailty, posture, and gestalt suggestive of old age may indicate higher disease risk [41]. In addition, labels are scarce as follow-up information (diagnosis dates, dates of death, etc.) is protected health information. Here, self- and semi-supervised techniques may improve risk prediction by using unlabeled data to improve label efficiency.

Chest radiographs (x-ray or CXR) are an ideal test-bed for risk prediction approaches because they are the most common diagnostic imaging test [32]. Studies have shown that

deep learning models can accurately interpret CXRs [5], and self-supervised techniques [34] improve CXR interpretation beyond transfer learning [37]. These efforts have been supported by the public release of large datasets with radiologists' interpretation of CXRs [17,40,4,19] (> 1 million total images). For risk prediction, these datasets are "unlabeled" in that there is no follow-up information. It is not yet known whether self- and semi-supervised techniques can leverage such data to improve label efficiency.

In this study, we evaluate self- and semi-supervised pretraining techniques for predicting mortality risk from CXRs. Our specific contributions are:

- We evaluate pretraining strategies using target variables with varying class imbalance.
- We investigate the generalizability of representations in an external validation dataset.
- We assess whether representations can predict disease history and risk factors.
- We explore the impact of image resolution on learned representations

## 2. Related Work

### 2.1. Self-supervised learning approaches

Self-supervised learning specifies a pre-training task on unlabeled datasets to improve performance on a target task with limited labeled data [15]. Most self-supervised learning strategies fall into 1) autoencoder/bottleneck and 2) contrastive learning-based approaches.

#### 2.1.1. AUTOENCODER-BASED APPROACHES

Autoencoders have two parts: 1) an "encoder" network that compresses the input image into a low-dimensional encoding and 2) a subsequent "decoder" model that reconstructs the original input image from the encoding [35, 43]. In [43], the authors combine a masked autoencoder (randomly occluded input) with a vision transformer [21] to improve classification of thoracic diseases beyond contrastive learning and ImageNet pretrained models; however, this study only had internal validation. In [35], the authors used a convolutional autoencoder to predict lung nodule malignancy from chest CT images and found a modest improvement over training from scratch. In [14], the authors show that more generalizable representations are obtained via a variational autoencoder trained on both labeled and unlabeled data with self-ensembling [23]; however, this work lacked external validation.

#### 2.1.2. CONTRASTIVE LEARNING APPROACHES

In contrastive learning, [12] ([Appendix: Contrastive Learning Methodology](#)), a model is trained to create image representations such that "positive pairs" (e.g., images from the same patient) have similar representations and "negative pairs" (e.g., images from different patients) have dissimilar representations [2,39,15,16]. Contrastive-learning improves performance on natural image classification tasks [8, 42]; however, sampling negative pairs has quadratic time complexity. Some use large batch sizes so that the model sees a diversity of negative pairs at each gradient update; however, this is GPU-memory intensive.

Others have proposed using a "memory bank" approach where representations of previously sampled images are stored. Then, representations from the current mini-batch are

"negative pairs" with these stored representations. Thus, the min-batch size is decoupled with the size of the memory bank. One such implementation is momentum contrast or MoCo [15], further described in [Appendix: MoCo Methodology](#)

Some approaches avoid using negative pairs entirely (BYOL, DINO, etc.) [6,13]. Instead, a teacher and student network receive augmented views of the same image, and the student must output a "prediction" that matches the teacher's prediction. Typically, the teacher is a moving average of previous student networks.

## 2.2. Comparisons of self-supervised and transfer-based pretraining

One study compared fully-supervised ImageNet pretraining vs. self-supervised pretraining, including SimCLR, SwAV (Swapping Assignments between multiple Views of the same image) [7], DINO [39], and an ensemble approach (Dynamic Visual Meta-Embedding - DVME) on medical image interpretation tasks. For CXR interpretation, no method consistently outperformed; however, self-supervised learning consistently outperformed transfer learning from ImageNet. It is unknown whether these results hold when using in-domain pretraining or in risk prediction tasks. In [2], the authors combined semi-supervised learning with end-to-end contrastive learning as a pretraining method. They compared two image augmentation methods: MICILe (two crops of the same image) vs. SimCLR (rotation, zoom, etc. of the same image). No difference was observed in CXR interpretation tasks. Another work compared [37] a modified MoCo pretrained on CheXpert vs. pretrained on ImageNet. Models were fine-tuned on CheXpert and Shenzhen hospital CXR datasets using 1) an additional linear layer or 2) end-to-end fine-tuning. MoCo models pretrained on CXRs performed better than ImageNet pretrained for all tested label fractions.

These results are corroborated by findings [10] that demonstrate that the pretraining task domain and the quality of the pre-training data are crucial factors for performance. Findings in medical imaging tasks [30] show that simple architectures trained entirely from scratch outperform large models pretrained using ImageNet. To our knowledge, no studies have tested pretraining strategies on risk prediction from medical imaging.

## 3. Methods

### 3.1. Datasets

In our study, we use two imaging datasets for pretraining: CheXpert [17] and NIH CXR-14 [40] ([Appendix Figure A.6](#)). CheXpert contains 224,316 CXRs taken at Stanford Hospital between October 2002 and July 2017. NIH CXR-14 contains CXRs taken at the NIH Clinical Center between 1992 and 2015 (108,948 images from 32,717 patients). Only frontal, posterior-anterior CXRs from patients aged 18 to 100 years were included (29419 CXRs from CheXpert and 64628 from NIH CXR-14). Since no follow-up is available, we use age, sex, and acute findings ([Appendix I](#)) from the radiologist's read for semi-supervised pretraining. For hyperparameter optimization, CheXpert and NIH CXR-14 were split into training ( $N = 74984$ ) and tuning ( $N = 19063$ ) datasets using a random 80%-20% split by patient. These datasets are used solely for pre-training.

All models were fine-tuned using data ([Appendix Figure A.5](#)) from the Prostate, Lung, Colorectal, and Ovarian cancer screening trial (PLCO) [27,29]. PLCO was a randomized

trial where adults 55-74 years were randomized to either a CXR or control (no imaging) with a maximum of 18 years of follow-up. The test dataset includes CXRs from PLCO (40,000  $T_{min}$  - earliest CXR for each participant) and the CXR arm of the National Lung Screening Trial (NLST; 5,414  $T_{min}$  CXRs) [1]. The NLST enrolled adults 55-77 years who had a heavy smoking history. NLST participants had a maximum of 12 years of follow-up. Models were trained to predict all-cause mortality 1 and 12 years after the CXR. Detailed cohort characteristics for all datasets are available in Appendix J.

### 3.2. Pre-training approaches

We compare several pre-training approaches: semi- and self-supervised autoencoder, semi- and self-supervised Patient-Centered Learning of Representations (PCLR), semi- and self-supervised MoCo, transfer learning, and training from scratch.

#### 3.2.1. SEMI-SUPERVISED AUTOENCODER ARCHITECTURE

The Semi-Supervised Autoencoder architecture has three components ([Figure 1](#)):

1. An image encoder  $f(\cdot)$ , which given input image  $x_i$ , outputs a 512-dimensional encoding  $f(x_i) = h_i$ . The encoder consists of 4 convolutional blocks, each with a convolutional layer (7x7 filters), batch normalization, ReLU activation, and max-pooling (3x3 window and 2x2 stride) ([Figure 1](#)). This architecture was previously shown to outperform transfer learning from ImageNet in medical image interpretation [30].
2. A prediction module, which uses image encodings  $h_i$  to classify 14 radiologist findings, (see Section 3.1) sex, and a continuous estimate of age. This encourages representations useful to identify important pathology and demographics.
3. An image decoder  $g(\cdot)$ , which reconstructs the input image  $x_i$  given encoding  $h_i$ . The decoder has 4 backward basic blocks, all with upsampling, batch norm, ReLU activation, and last layer sigmoid activation ([Figure 1](#)).

#### 3.2.2. SEMI-SUPERVISED AUTOENCODER LOSS

The model weights are optimized using a three-part loss function:

1. First, reconstruction mean-squared error (MSE) of predicted vs. original images.
2. Second, a composite cross-entropy loss for multi-label classification (findings and sex) and MSE loss for age.
3. Third, an L1 Regularization on the encodings  $h_i$  [3].

The overall loss is given by:

$$Loss_{autoencoder} = \lambda_{recon} * recon_{x, \hat{x}} + \lambda_{reg} * (reg_{h_i} + cls_{h_i}) + \lambda_{norm} * norm \quad (1)$$

Here,  $\lambda_{recon}$ ,  $\lambda_{reg}$ , and  $\lambda_{norm}$  control the contributions of reconstruction, classification, and normalization to the overall loss. We chose (1, 20, 0.0001) as defaults to scale each equally. We tested the sensitivity of  $\lambda$  and found little impact ([Hyperparameter Sensitivity Analysis](#)).

The **Self-Supervised Autoencoder** has the same architecture but no prediction module and no cross-entropy loss component.

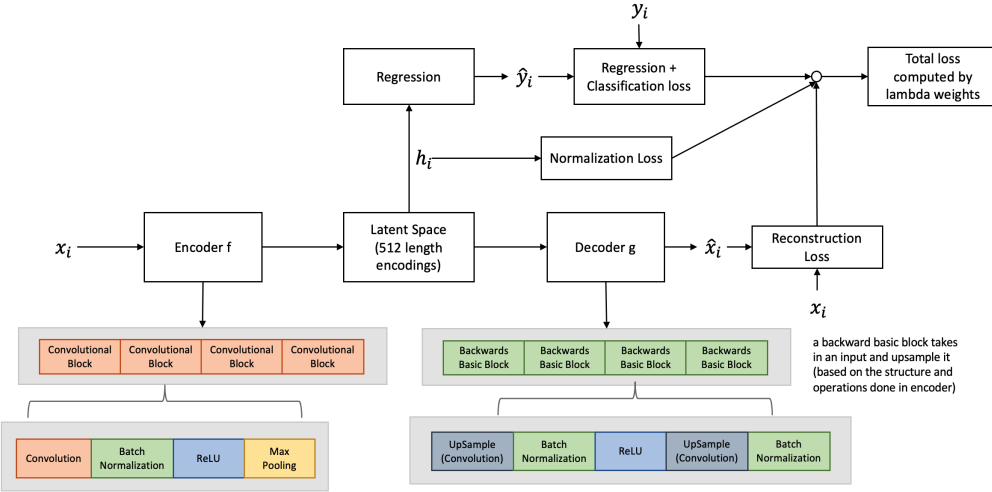


Figure 1: Autoencoder architecture for an input CXR  $x_i$  and corresponding label  $y_i$ .

### 3.2.3. OTHER APPROACHES

**Transfer Learning & Train From Scratch** We tested transfer learning [38], where the pretraining task was to predict sex, the radiologist findings, and age. We also tested a model that was trained with randomly initialized weights on the PLCO training dataset ("train from scratch"). All approaches use the encoder architecture described above (Section 3.3.1). The transfer learning loss was just the composite cross-entropy and multi-label classification loss (see 3.3.2). A binary cross-entropy loss was used for training from scratch.

**Contrastive Learning** We used two implementations of contrastive learning: 1) an end-to-end Patient Contrastive Learning of Representations (PCLR) [12] and Momentum Contrast-CXR (MoCo-CXR) [37]. A detailed explanation of both approaches are in [Appendix: Contrastive Learning Methodology](#).

### 3.2.4. MODEL OPTIMIZERS AND OPTIMIZATIONS

All models were trained for 100 epochs, batch size 64, using the Adam optimizer [20] with a maximum learning rate of  $1e-5$  and the 1-cycle policy [36]. For each strategy, the model with the lowest validation loss during training was chosen for downstream experiments.

## 3.3. Experiments

Experimental steps are outlined in [Figure 2](#). After pretraining, we perform forward propagation on all PLCO and NLST images. The extracted encodings from PLCO participants are divided into training and testing sets (80% - 20% split). The testing set ( $N = 40,000$ ) is fixed for all experiments, and we randomly sample from the training set to generate 15 datasets for each sample size (40000, 20000, 10000, 5000, 2000, 1000, 500, and 200). Identical training

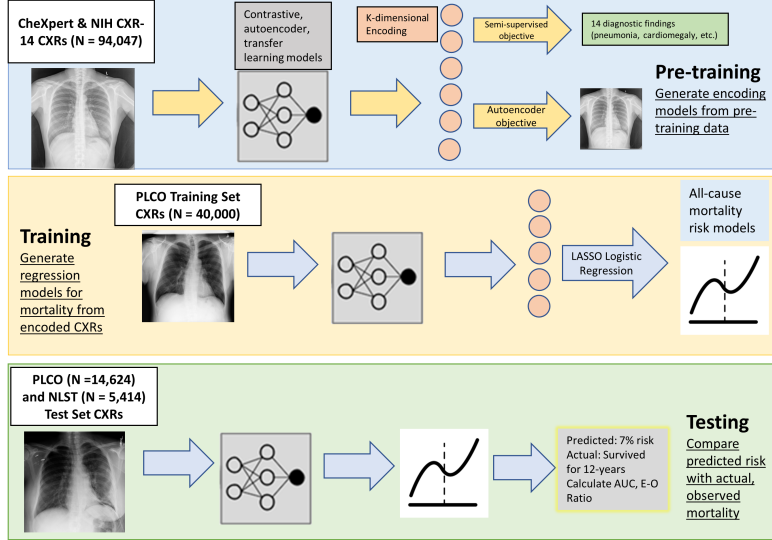


Figure 2: Overview of experimental procedure.

and testing sets were used for all models to ensure fairness. We test the effect of imbalanced outcomes by training on 1-year (event rate 0.456%) and 12-year mortality (14.205%). We separately tested the effect of random weight initializations during pretraining using 5 random initializations for each model (Appendix K).

PLCO encodings were scaled and centered and 0 variance encodings were removed. Testing encodings were transformed using training data statistics. A LASSO logistic regression was trained to predict mortality risk using extracted image encodings.  $\lambda$  for LASSO was selected using cross-validation AUC [22]. Pretraining strategies were assessed using discrimination and calibration of downstream predictions. We used mean AUC for discrimination and mean E/O Ratio (expected/observed ratio) for calibration across the 15 trials for each training set size and mortality time horizon.

## 4. Results

### 4.1. Effect of pre-training strategy on discriminative accuracy

In [Figure 3](#) and [Figure 4](#), we compared discrimination for 12- and 1-year all-cause mortality. We found that semi-supervision outperformed self-supervised models in external validation for most training set sizes. In particular, the semi-supervised autoencoder and transfer learning from diagnostic labels (with no self-supervision) had highest AUC when the training set was small, while semi-supervised contrastive learning excelled with  $>5000$  samples and for 1-year mortality. Among the fully self-supervised models, contrastive learning (PCLR) performed the closest to semi-supervised methods and even outperformed semi-supervised MoCo in external validation for 12-year mortality. Often, training a model from scratch outperformed self-supervised approaches. For all approaches, the gap between internal and external validation AUC was higher for 12-year mortality than 1-year, potentially due to

overfitting. This gap was still pronounced for 1-year mortality for transfer learning, self-supervised PCLR, and training from scratch (> 5% drop in AUC) ([Figure 3](#) and [Figure 4](#)).

In a sensitivity analysis, we tested whether the differences between internal and external validation performance could be explained by differences in smoking history. When limiting the internal testing dataset to only individuals meeting eligibility criteria for the external validation dataset, we found that discrimination performance was similar between NLST and PLCO heavy smokers for 1-year mortality ([Appendix I](#)), This difference was larger for 12-year mortality; however, this suggests that some of the drop in performance in NLST is due to increased smoking intensity, not generalization error. Additional sensitivity analyses showed similar results when changing the image resolution to 128x128 and 320x320 ([Appendix L](#)), when varying the random weight initialization ([Appendix K](#)), and when changing the downstream classification model ([Appendix H](#)).

#### 4.2. Effect of pretraining strategy on calibration

We assessed calibration using the E-O Ratio ([Appendix Table D.2](#), [Appendix Table D.3](#), [Appendix Table D.4](#), [Appendix Table D.5](#)). In internal validation, we find that all models are well-calibrated for 12-year mortality (except train from scratch which over-predicted risk), and all models over-predicted risk for 1-year mortality. In external validation, the semi-supervised autoencoder and transfer learning were well-calibrated, especially for 1-year mortality. Contrastive learning approaches consistently under-predicted risk for both 12- and 1-year mortality. Self-supervised models followed a similar trend, except contrastive learning alone was well-calibrated in 12-year external validation, whereas the self-supervised autoencoder was well-calibrated for 1-year external validation. In general, semi-supervised models had better calibration in external validation than their self-supervised counterparts.

#### 4.3. Comparison of pretraining strategies to predict risk factors

To assess whether some representations were more suited to certain disease processes (e.g., cardiovascular vs. lung disease), we used generated encodings to develop prediction models for prevalent risk factors, disease history, and radiologist findings ([Appendix: Intermediate Risk Factors Results](#)). We found that the semi-supervised autoencoder predicted all risk factors better than other pretraining approaches in internal and external validation.

### 5. Discussion

In this study, we tested pretraining approaches to use unlabeled or off-labeled data to predict mortality risk from CXR images. Our major findings were that 1) using off-target, but relevant labels in pre-training is better than self-supervised and no pretraining, 2) self-supervised pretraining is no better than training from scratch in most downstream tasks ([Figures 3 and 4](#)), and 3) semi-supervised autoencoder and transfer learning representations were strongly associated with risk factors, suggesting that these representations may be well-suited for more general tasks ([Appendix G](#)). We found that autoencoder representations were robust to hyperparameter choices and were generally well-calibrated ([Appendix D](#)). In sensitivity analyses, we found that the reduced external validation performance for

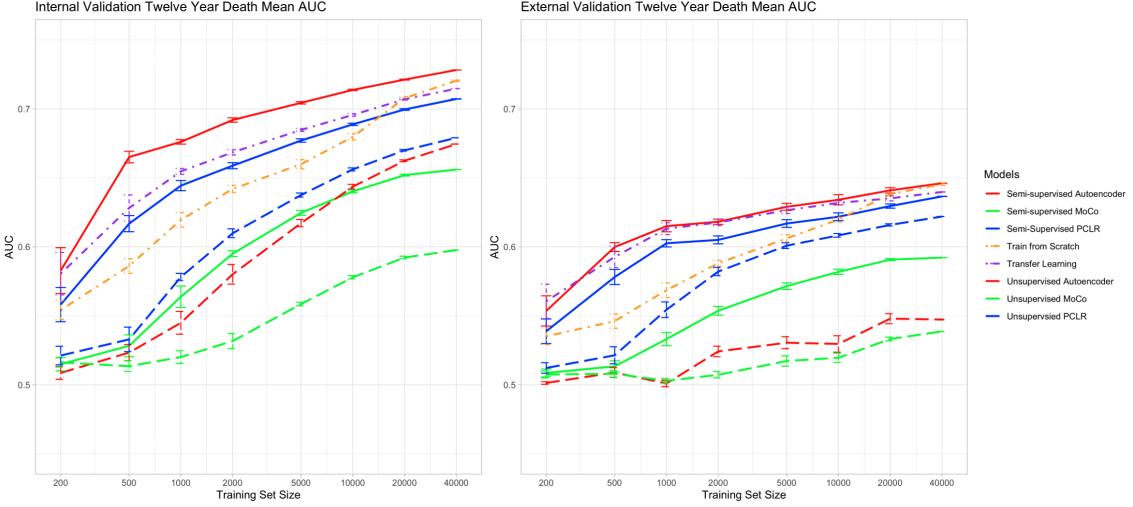


Figure 3: Comparison of approaches to predict 12-year mortality. Training set size (x-axis) vs. mean AUC (y-axis) in PLCO internal (left) and NLST external validation (right) data.

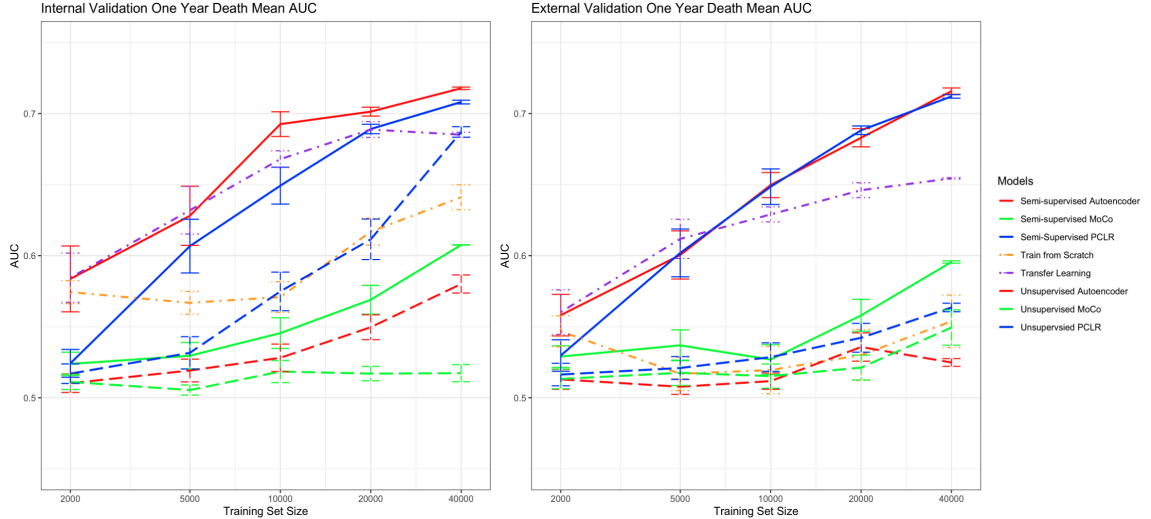


Figure 4: Comparison of approaches to predict 1-year mortality. Training set size (x-axis) vs. mean AUC (y-axis) in PLCO internal (left) and NLST external validation (right) data.

semi-supervised approaches was due to differences in participant characteristics, not generalization error (Appendix I). Unlike previous studies of medical image pretraining, our study focuses on risk prediction and has external validation data. The semi-supervised autoencoder is publicly available at <https://github.com/circ-ml/cxr-encoder>. Limitations of this study should be considered. We used one base architecture that showed success in CXR interpretation tasks, and we tested only CXR images; future studies should explore more architectures and other imaging modalities. Our primary outcome was all-cause mortality;

however, performance in predicting other intermediate outcomes (heart attack, lung cancer) is unknown. Lastly, our cohorts were predominantly non-Hispanic white individuals.

## Acknowledgments

We would like to thank The National Cancer Institute and the American College of Radiology Imaging Network (ACRIN) for access to trial data, and Stanford University and the National Institutes of Health for access to the chest x-ray datasets. We also thank the fastai and PyTorch communities for the development of open-source software. The statements contained herein are solely those of the authors and do not represent or imply concurrence or endorsements by any named organizations.

## References

Reduced lung-cancer mortality with low-dose computed tomographic screening. *New England Journal of Medicine*, 365(5):395–409, August 2011. doi: 10.1056/nejmoa1102873. URL <https://doi.org/10.1056/nejmoa1102873>.

Shekoofeh Azizi, Basil Mustafa, Fiona Ryan, Zachary Beaver, Jan Freyberg, Jonathan Deaton, Aaron Loh, Alan Karthikesalingam, Simon Kornblith, Ting Chen, Vivek Nataraajan, and Mohammad Norouzi. Big self-supervised models advance medical image classification, 2021. URL <https://arxiv.org/abs/2101.05224>.

Dor Bank, Noam Koenigstein, and Raja Giryes. Autoencoders, 2020. URL <https://arxiv.org/abs/2003.05991>.

Aurelia Bustos, Antonio Pertusa, Jose-Maria Salinas, and Maria de la Iglesia-Vayá. PadChest: A large chest x-ray image dataset with multi-label annotated reports. *Medical Image Analysis*, 66:101797, December 2020. ISSN 1361-8415. doi: 10.1016/j.media.2020.101797.

Erdi Çalli, Ecem Sogancioglu, Bram van Ginneken, Kicky G. van Leeuwen, and Keelin Murphy. Deep learning for chest X-ray analysis: A survey. *Medical Image Analysis*, 72: 102125, August 2021. ISSN 1361-8415. doi: 10.1016/j.media.2021.102125.

Mathilde Caron, Hugo Touvron, Ishan Misra, Hervé Jegou, Julien Mairal, Piotr Bojanowski, and Armand Joulin. Emerging Properties in Self-Supervised Vision Transformers. In *2021 IEEE/CVF International Conference on Computer Vision (ICCV)*, pages 9630–9640, Montreal, QC, Canada, October 2021a. IEEE. ISBN 978-1-66542-812-5. doi: 10.1109/ICCV48922.2021.00951.

Mathilde Caron, Hugo Touvron, Ishan Misra, Hervé Jegou, Julien Mairal, Piotr Bojanowski, and Armand Joulin. Emerging properties in self-supervised vision transformers, 2021b. URL <https://arxiv.org/abs/2104.14294>.

Ting Chen, Simon Kornblith, Mohammad Norouzi, and Geoffrey Hinton. A simple framework for contrastive learning of visual representations, 2020a. URL <https://arxiv.org/abs/2002.05709>.

Ting Chen, Simon Kornblith, Mohammad Norouzi, and Geoffrey E. Hinton. A simple framework for contrastive learning of visual representations. *CoRR*, abs/2002.05709, 2020b. URL <https://arxiv.org/abs/2002.05709>.

Elijah Cole, Xuan Yang, Kimberly Wilber, Oisin Mac Aodha, and Serge Belongie. When does contrastive visual representation learning work?, 2021. URL <https://arxiv.org/abs/2105.05837>.

Jia Deng, Wei Dong, Richard Socher, Li-Jia Li, Kai Li, and Li Fei-Fei. ImageNet: A large-scale hierarchical image database. In *2009 IEEE Conference on Computer Vision and Pattern Recognition*, pages 248–255, June 2009. doi: 10.1109/CVPR.2009.5206848.

Nathaniel Diamant, Erik Reinertsen, Steven Song, Aaron D. Aguirre, Collin M. Stultz, and Puneet Batra. Patient contrastive learning: A performant, expressive, and practical approach to electrocardiogram modeling. *PLOS Computational Biology*, 18(2):e1009862, 2022. doi: 10.1371/journal.pcbi.1009862.

Jean-Bastien Grill, Florian Strub, Florent Altché, Corentin Tallec, Pierre Richemond, Elena Buchatskaya, Carl Doersch, Bernardo Avila Pires, Zhaohan Guo, Mohammad Gheshlaghi Azar, Bilal Piot, koray kavukcuoglu, Remi Munos, and Michal Valko. Bootstrap Your Own Latent - A New Approach to Self-Supervised Learning. In *Advances in Neural Information Processing Systems*, volume 33, pages 21271–21284. Curran Associates, Inc., 2020.

Prashnna Kumar Gyawali, Zhiyuan Li, Sandesh Ghimire, and Linwei Wang. Semi-supervised Learning by Disentangling and Self-ensembling over Stochastic Latent Space. In Dinggang Shen, Tianming Liu, Terry M. Peters, Lawrence H. Staib, Caroline Essert, Sean Zhou, Pew-Thian Yap, and Ali Khan, editors, *Medical Image Computing and Computer Assisted Intervention – MICCAI 2019*, Lecture Notes in Computer Science, pages 766–774, Cham, 2019. Springer International Publishing. ISBN 978-3-030-32226-7. doi: 10.1007/978-3-030-32226-7\_85.

Kaiming He, Haoqi Fan, Yuxin Wu, Saining Xie, and Ross Girshick. Momentum contrast for unsupervised visual representation learning, 2019. URL <https://arxiv.org/abs/1911.05722>.

R Devon Hjelm, Alex Fedorov, Samuel Lavoie-Marchildon, Karan Grewal, Phil Bachman, Adam Trischler, and Yoshua Bengio. Learning deep representations by mutual information estimation and maximization, 2018. URL <https://arxiv.org/abs/1808.06670>.

Jeremy Irvin, Pranav Rajpurkar, Michael Ko, Yifan Yu, Silviana Ciurea-Ilcus, Chris Chute, Henrik Marklund, Behzad Haghgoo, Robyn Ball, Katie Shpanskaya, Jayne Seekins, David A. Mong, Safwan S. Halabi, Jesse K. Sandberg, Ricky Jones, David B. Larson, Curtis P. Langlotz, Bhavik N. Patel, Matthew P. Lungren, and Andrew Y. Ng. CheXpert: A Large Chest Radiograph Dataset with Uncertainty Labels and Expert Comparison. *Proceedings of the AAAI Conference on Artificial Intelligence*, 33(01):590–597, July 2019. ISSN 2374-3468. doi: 10.1609/aaai.v33i01.3301590.

Fabian Isensee, Paul F. Jaeger, Simon A. A. Kohl, Jens Petersen, and Klaus H. Maier-Hein. nnU-Net: A self-configuring method for deep learning-based biomedical image segmentation. *Nature Methods*, 18(2):203–211, February 2021. ISSN 1548-7105. doi: 10.1038/s41592-020-01008-z.

Alistair E. W. Johnson, Tom J. Pollard, Seth J. Berkowitz, Nathaniel R. Greenbaum, Matthew P. Lungren, Chih-ying Deng, Roger G. Mark, and Steven Horng. MIMIC-CXR, a de-identified publicly available database of chest radiographs with free-text reports. *Scientific Data*, 6(1):317, December 2019. ISSN 2052-4463. doi: 10.1038/s41597-019-0322-0.

Diederik P. Kingma and Jimmy Ba. Adam: A method for stochastic optimization, 2014. URL <https://arxiv.org/abs/1412.6980>.

Alexander Kolesnikov, Alexey Dosovitskiy, Dirk Weissenborn, Georg Heigold, Jakob Uszkoreit, Lucas Beyer, Matthias Minderer, Mostafa Dehghani, Neil Houlsby, Sylvain Gelly, Thomas Unterthiner, and Xiaohua Zhai. An Image is Worth 16x16 Words: Transformers for Image Recognition at Scale. 2021.

Knut Kvaal and Jean A. McEwan. Analysing complex sensory data by non-linear artificial neural networks. In Tormod Naes and Einar Røvik, editors, *Multivariate analysis of data in sensory science*, volume 16 of *Data Handling in Science and Technology*, pages 103–133. Elsevier, 1996. doi: [https://doi.org/10.1016/S0922-3487\(96\)80028-1](https://doi.org/10.1016/S0922-3487(96)80028-1). URL <https://www.sciencedirect.com/science/article/pii/S0922348796800281>.

Samuli Laine and Timo Aila. Temporal Ensembling for Semi-Supervised Learning, March 2017.

Geert Litjens, Thijs Kooi, Babak Ehteshami Bejnordi, Arnaud Arindra Adiyoso Setio, Francesco Ciompi, Mohsen Ghafoorian, Jeroen A.W.M. van der Laak, Bram van Ginneken, and Clara I. Sánchez. A survey on deep learning in medical image analysis. *Medical Image Analysis*, 42:60–88, 2017. ISSN 1361-8415. doi: 10.1016/j.media.2017.07.005.

Michael T. Lu, Alexander Ivanov, Thomas Mayrhofer, Ahmed Hosny, Hugo J. W. L. Aerts, and Udo Hoffmann. Deep Learning to Assess Long-term Mortality From Chest Radiographs. *JAMA Network Open*, 2(7):e197416, July 2019. ISSN 2574-3805. doi: 10.1001/jamanetworkopen.2019.7416.

Michael T. Lu, Vineet K. Raghu, Thomas Mayrhofer, Hugo J. W. L. Aerts, and Udo Hoffmann. Deep Learning Using Chest Radiographs to Identify High-Risk Smokers for Lung Cancer Screening Computed Tomography: Development and Validation of a Prediction Model. *Annals of Internal Medicine*, 173(9):704–713, November 2020. ISSN 1539-3704. doi: 10.7326/M20-1868.

Martin M. Oken, William G. Hocking, Paul A. Kvale, Gerald L. Andriole, Saundra S. Buys, Timothy R. Church, E. David Crawford, Mona N. Fouad, Claudine Isaacs, Douglas J. Reding, Joel L. Weissfeld, Lance A. Yokochi, Barbara O’Brien, Lawrence R. Ragard, Joshua M. Rathmell, Thomas L. Riley, Patrick Wright, Neil Caparaso, Ping Hu, Grant Izmirlian, Paul F. Pinsky, Philip C. Prorok, Barnett S. Kramer, Anthony B. Miller,

John K. Gohagan, Christine D. Berg, and for the PLCO Project Team. Screening by chest radiograph and lung cancer mortality. *JAMA*, 306(17):1865, November 2011. doi: 10.1001/jama.2011.1591. URL <https://doi.org/10.1001/jama.2011.1591>.

Ryan Poplin, Avinash V. Varadarajan, Katy Blumer, Yun Liu, Michael V. McConnell, Greg S. Corrado, Lily Peng, and Dale R. Webster. Prediction of cardiovascular risk factors from retinal fundus photographs via deep learning. *Nature Biomedical Engineering*, 2(3): 158–164, March 2018. ISSN 2157-846X. doi: 10.1038/s41551-018-0195-0.

Philip C. Prorok, Gerald L. Andriole, Robert S. Bresalier, Saundra S. Buys, David Chia, E. David Crawford, Ronald Fogel, Edward P. Gelmann, Fred Gilbert, Marsha A. Hasson, Richard B. Hayes, Christine Cole Johnson, Jack S. Mandel, Albert Oberman, Barbara O'Brien, Martin M. Oken, Sameer Rafla, Douglas Reding, Wilmer Rutt, Joel L. Weissfeld, Lance Yokochi, and John K. Gohagan. Design of the prostate, lung, colorectal and ovarian (PLCO) cancer screening trial. *Controlled Clinical Trials*, 21(6):273S–309S, December 2000. doi: 10.1016/s0197-2456(00)00098-2. URL [https://doi.org/10.1016/s0197-2456\(00\)00098-2](https://doi.org/10.1016/s0197-2456(00)00098-2).

Maithra Raghu, Chiyuan Zhang, Jon Kleinberg, and Samy Bengio. Transfusion: Understanding transfer learning for medical imaging, 2019. URL <https://arxiv.org/abs/1902.07208>.

Vineet K. Raghu, Jakob Weiss, Udo Hoffmann, Hugo J.W.L. Aerts, and Michael T. Lu. Deep learning to estimate biological age from chest radiographs. *JACC: Cardiovascular Imaging*, 14(11):2226–2236, November 2021. doi: 10.1016/j.jcmg.2021.01.008. URL <https://doi.org/10.1016/j.jcmg.2021.01.008>.

Elaine Ron. CANCER RISKS FROM MEDICAL RADIATION. *Health Physics*, 85(1):47, July 2003. ISSN 0017-9078.

Farah E. Shamout, Yiqiu Shen, Nan Wu, Aakash Kaku, Jungkyu Park, Taro Makino, Stanisław Jastrzębski, Jan Witowski, Duo Wang, Ben Zhang, Siddhant Dogra, Meng Cao, Narges Razavian, David Kudlowitz, Lea Azour, William Moore, Yvonne W. Lui, Yindalon Aphinyanaphongs, Carlos Fernandez-Granda, and Krzysztof J. Geras. An artificial intelligence system for predicting the deterioration of COVID-19 patients in the emergency department. *npj Digital Medicine*, 4(1):1–11, May 2021. ISSN 2398-6352. doi: 10.1038/s41746-021-00453-0.

Saeed Shurrob and Rehab Duwairi. Self-supervised learning methods and applications in medical imaging analysis: A survey. *PeerJ Computer Science*, 8:e1045, July 2022. ISSN 2376-5992. doi: 10.7717/peerj-cs.1045.

Francisco Silva, Tania Pereira, Julieta Fraude, José Mendes, Claudia Freitas, Venceslau Hespanhol, José Luis Costa, António Cunha, and Hélder P. Oliveira. Pre-training autoencoder for lung nodule malignancy assessment using CT images. *Applied Sciences*, 10(21): 7837, November 2020. doi: 10.3390/app10217837. URL <https://doi.org/10.3390/app10217837>.

Leslie N. Smith. A disciplined approach to neural network hyper-parameters: Part 1 - learning rate, batch size, momentum, and weight decay. *CoRR*, abs/1803.09820, 2018. URL <http://arxiv.org/abs/1803.09820>.

Hari Sowrirajan, Jingbo Yang, Andrew Y. Ng, and Pranav Rajpurkar. Moco-cxr: Moco pretraining improves representation and transferability of chest x-ray models, 2020. URL <https://arxiv.org/abs/2010.05352>.

Chuanqi Tan, Fuchun Sun, Tao Kong, Wenchang Zhang, Chao Yang, and Chunfang Liu. A survey on deep transfer learning. *CoRR*, abs/1808.01974, 2018. URL <http://arxiv.org/abs/1808.01974>.

Tuan Truong, Sadegh Mohammadi, and Matthias Lenga. How transferable are self-supervised features in medical image classification tasks?, 2021. URL <https://arxiv.org/abs/2108.10048>.

Xiaosong Wang, Yifan Peng, Le Lu, Zhiyong Lu, Mohammad Bagheri, and Ronald M. Summers. ChestX-ray8: Hospital-Scale Chest X-Ray Database and Benchmarks on Weakly-Supervised Classification and Localization of Common Thorax Diseases. In *Proceedings of the IEEE Conference on Computer Vision and Pattern Recognition*, pages 2097–2106, 2017.

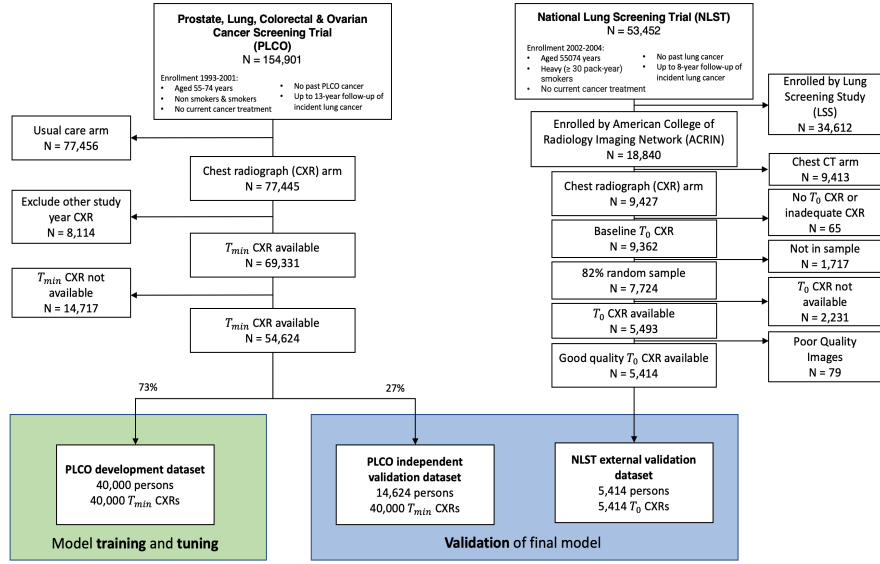
Jakob Weiss, Jana Taron, Zexi Jin, Thomas Mayrhofer, Hugo J. W. L. Aerts, Michael T. Lu, and Udo Hoffmann. Radiologists can visually predict mortality risk based on the gestalt of chest radiographs comparable to a deep learning network. *Scientific Reports*, 11(1):19586, October 2021. ISSN 2045-2322. doi: 10.1038/s41598-021-99107-0.

Zhirong Wu, Yuanjun Xiong, Stella X. Yu, and Dahua Lin. Unsupervised Feature Learning via Non-Parametric Instance Discrimination. In *Proceedings of the IEEE Conference on Computer Vision and Pattern Recognition*, pages 3733–3742, 2018.

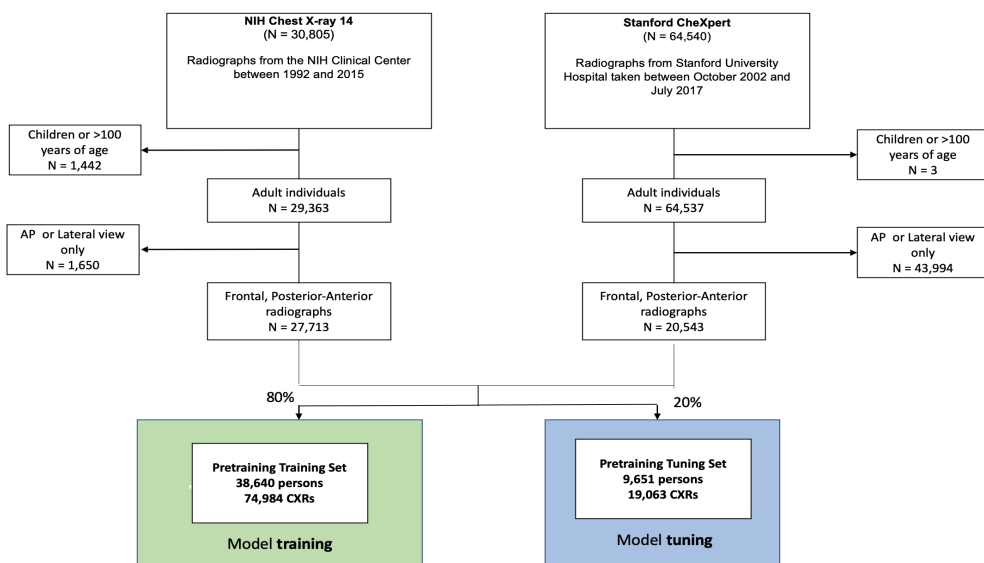
Lei Zhou, Huidong Liu, Joseph Bae, Junjun He, Dimitris Samaras, and Prateek Prasanna. Self pre-training with masked autoencoders for medical image analysis, 2022. URL <https://arxiv.org/abs/2203.05573>.

## Appendix A. Image Preprocessing

Image preprocessing steps followed our previous work [31]. For PLCO CXRs, we converted original TIF files to PNG with a short-axis dimension of 512 using ImageMagick. A previously developed CNN was used to identify rotated PLCO radiographs and ImageMagick was used to correct these. Similar preprocessing steps were used for NLST, though first CXRs were converted from native DICOM to TIF using the DCMTK toolbox. All input PNG images to the model were resized to 224 x 224 pixels using random cropping along the longer axis. Random data augmentation was used during training, including up to 5 degrees of rotation, up to 20% zoom in/out, and up to 50% brightness and contrast adjustment. No augmentation was used during validation and testing.



Appendix Figure A.5: CONSORT diagram for PLCO and NLST training and testing datasets. Only the earliest ( $T_{min}$ ) CXR from each patient was used.



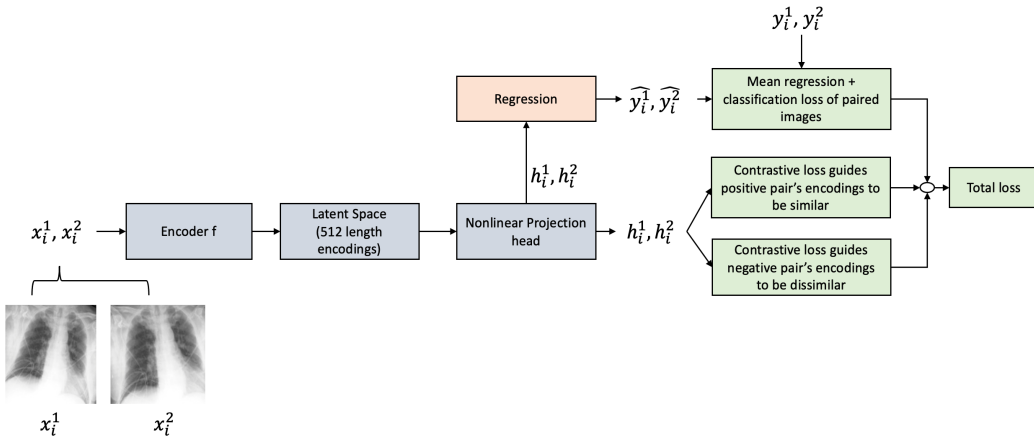
Appendix Figure A.6: CONSORT diagram for pretraining datasets NIH Chest X-ray 14 and CheXpert. Only adult, frontal, and posterior-anterior radiographs are kept.

## Appendix B. End-to-end Contrastive Learning Methodology (PCLR)

We implemented the same data selection method used in PCLR [12] but with a different model architecture. For training, first, a mini-batch of images from unique patients was randomly sampled. To create "positive pairs," a second image from each of these patients was randomly sampled, otherwise, an augmented version of the first image was used. All individual images were randomly transformed as described in Appendix A

The Contrastive Learning approach used an identical image encoder architecture as the Autoencoder-Classifier but trained with different loss functions and input data structure. The major differences in this approach are as follows:

1. A Nonlinear projection head using the ReLU activation function that maintains 512-dimensional encodings and projects image encodings onto a nonlinear space. The results of [8] demonstrate that the incorporation of a nonlinear projection head leads to an improvement in the quality of the representation learned by contrastive learning models. The aim of the projection head is to learn a compact, meaningful and discriminative representation of the input data that can be effectively used in later downstream tasks.
2. A Contrastive loss function is used to train the encoder and projection head. Contrastive loss  $cl_{i,j}$  will be low for positive pairs and high for negative pairs, which encourages the model to generate similar encodings (based on cosine similarity) for CXRs from the same patient and dissimilar encodings for CXRs from different patients.



Appendix Figure B.7: Contrastive Learning model architecture for an input x-ray image pair  $(x_i^1, x_i^2)$  and corresponding label  $(y_i^1, y_i^2)$ .

**PCLR Loss** To make image encodings  $p(h_i)$  produced by the projection head  $p$  similar for positive pairs and dissimilar for negative pairs, we used the contrastive loss function introduced in SimCLR [9]. Let  $(z_i, z_j)$  be positive pairs, remaining  $(z_i, z_k)$  be negative pairs,

$\tau$  be the temperature of the similarity function, loss of a positive pair  $(z_i, z_j)$  (in total of  $N$  pairs of input) using cosine similarity  $sim$  as the distance between two encodings can be written as:

$$l_{i,j} = -\log \frac{\exp(sim(z_i, z_j)/\tau)}{\sum_{k=1}^{2N} \mathbb{1}_{k \neq i} \exp(sim(z_i, z_k)/\tau)} \quad (2)$$

Given a batch of  $M$  patients, we will have a total of  $2M$  encoded images and  $M$ -positive pairs. Two adjacent encoded images  $h_i, h_{i+1}$  will be positive pairs. Thus total loss will be the sum of all losses between positive pairs is:

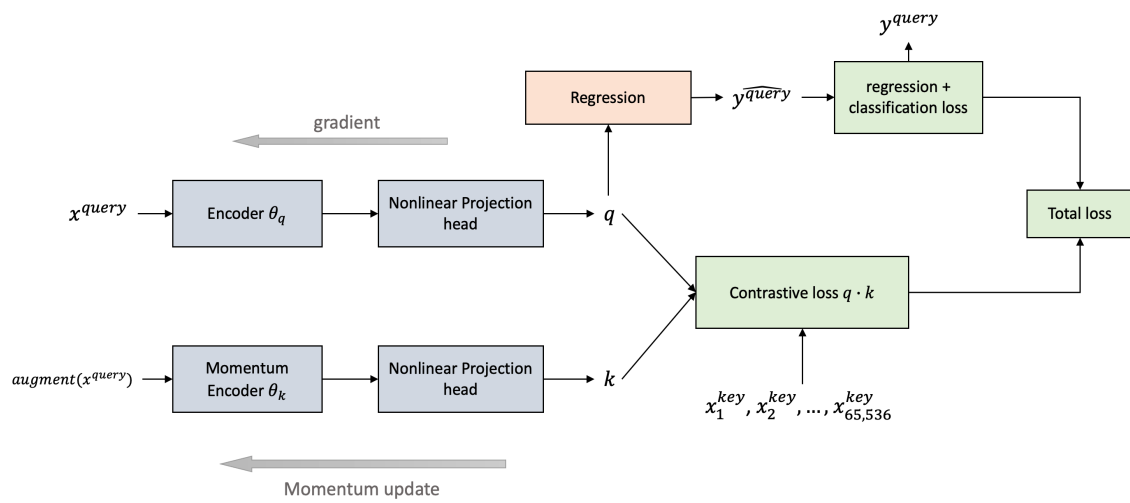
$$C_{batch} = \frac{1}{2M} \sum_{i=1}^M [l_{i,i+1}]_{i \in 2\mathbb{Z}} \quad (3)$$

## Appendix C. MoCo Methodology

We used the MoCo pretraining technique as described in [15] with a batch size of 32 anchor images. A heavy image augmentation technique, similar to the procedure used in SimCLR, is employed as a pretraining task.

The MoCo pre-training procedure is as follows [Figure C.8](#):

1. An image encoder  $\theta_q$  used to generate a 512-dimensional image encoding for anchor image (or query, which is the name used in [15]). The structure of this image encoder is the same as that of a complete autoencoder. The image encoding is then projected onto a 128-dimensional vector space using a nonlinear projection head, denoted by  $g(\cdot)$ .
2. A momentum encoder  $\theta_k$  is used to encode the positive and negative pair for the query. The structure of  $\theta_k$  is exactly the same as  $\theta_q$ , but no back-propagation is performed. The weights were updated using  $\theta_k \leftarrow m\theta_k + (1 - m)\theta_q$  [15] where  $m$  is the momentum hyperparameter which controls the speed of momentum encoder's update. We set  $m = 0.999$  as suggested.
3. A first-in-first-out (FIFO) queue, comprised of previous image encodings (keys), enqueues the latest mini-batch's encodings, and dequeues the earliest mini-batch's encodings. Since MoCo is more effective when the dictionary size is large, we used 65,536 for the queue size as suggested by the authors.
4. A contrastive loss function [Equation 2](#) was used to train the overall model with back-propagation performed only on the parameters of  $\theta_q$ . It uses the query image and its augmented version as a positive pair, which is encoded by  $\theta_k$ , and the rest of the keys in the queue as negative pairs. The softmax temperature was 0.07.



Appendix Figure C.8: Momentum Contrastive Learning model architecture for an input x-ray  $x^{query}$ , its augmented version as positive pair  $augment(x^{query})$ , and corresponding label  $y^{query}$ .

## Appendix D. Calibration of all-cause mortality risk estimates

Lambda	One-Year Death (PLCO)				Twelve-Year Death (NLST)			
	Amplified Classification Parameter	Amplified Image Reconstruction Parameter	Amplified Normalization Parameter	Original Parameter	Amplified Classification Parameter	Amplified Image Reconstruction Parameter	Amplified Normalization Parameter	Original Parameter
200	1.026(0.215)	1.027(0.212)	1.021(0.221)	1.031(0.211)	0.998(0.535)	1.104(0.921)	1.071(0.827)	1.04(0.513)
500	1.054(0.078)	1.056(0.08)	1.05(0.08)	1.047(0.079)	1.218(0.66)	0.925(0.584)	1.098(0.719)	1.137(0.672)
1000	1.014(0.067)	1.01(0.066)	1.009(0.07)	1.008(0.067)	1.601(0.83)	1.127(0.844)	1.285(0.646)	1.166(0.65)
2000	1.021(0.057)	1.024(0.055)	1.026(0.055)	1.023(0.057)	1.857(0.754)	1.229(0.685)	1.127(0.622)	1.483(0.696)
5000	1.025(0.032)	1.024(0.032)	1.024(0.03)	1.023(0.031)	1.433(0.42)	0.99(0.585)	0.631(0.239)	0.835(0.558)
10000	1.143(0.124)	1.136(0.116)	1.168(0.124)	1.262(0.311)	1.133(0.117)	1.03(0.013)	1.031(0.018)	1.034(0.021)
20000	1.227(0.085)	1.221(0.086)	1.224(0.103)	1.162(0.106)	1.223(0.086)	1.031(0.015)	1.033(0.017)	1.036(0.011)
40000	1.212(0.0)	1.206(0.0)	1.209(0.003)	1.187(0.102)	1.21(0.001)	1.029(0.0)	1.031(0.0)	1.031(0.0)

Appendix Table D.1: Calibration Results for Hyperparameter Sensitivity Analysis

PLCO	One-year death					Twelve-Year Death				
	Semi-Supervised Autoencoder	Semi-supervised PCLR	Transfer Learning	From Scratch	Semi-supervised MoCo	Semi-Supervised Autoencoder	Semi-supervised PCLR	Transfer Learning	From Scratch	Semi-supervised MoCo
200	N/A	N/A	N/A	N/A	N/A	1.024(0.21)	1.024(0.206)	1.018(0.116)	1.17(0.831)	1.027(0.211)
500	N/A	N/A	N/A	N/A	N/A	1.052(0.081)	1.052(0.079)	1.106(0.108)	1.142(0.179)	1.057(0.08)
1000	N/A	N/A	N/A	N/A	N/A	1.008(0.061)	1.003(0.066)	1.015(0.06)	1.141(0.115)	1.006(0.067)
2000	1.116(0.417)	1.114(0.412)	1.223(0.316)	1.881(1.59)	1.102(0.435)	1.022(0.057)	1.017(0.055)	1.039(0.036)	1.108(0.096)	1.016(0.058)
5000	1.222(0.249)	1.201(0.249)	1.23(0.259)	1.226(0.445)	1.207(0.252)	1.019(0.029)	1.021(0.033)	1.034(0.025)	1.078(0.054)	1.022(0.032)
10000	1.143(0.124)	1.136(0.116)	1.168(0.124)	1.262(0.311)	1.133(0.117)	1.03(0.013)	1.031(0.018)	1.034(0.021)	1.115(0.031)	1.031(0.016)
20000	1.227(0.085)	1.221(0.086)	1.224(0.103)	1.162(0.106)	1.223(0.086)	1.031(0.015)	1.033(0.017)	1.036(0.011)	1.112(0.026)	1.032(0.017)
40000	1.212(0.0)	1.206(0.0)	1.209(0.003)	1.187(0.102)	1.21(0.001)	1.029(0.0)	1.031(0.0)	1.031(0.0)	1.081(0.032)	1.031(0.0)

Appendix Table D.2: Calibration of semi-supervised and supervised models in the PLCO dataset. Results are not available for some smaller training sets due to insufficient events.

NLST	One-year death					Twelve-Year Death				
	Semi-Supervised Autoencoder	Semi-supervised PCLR	Transfer Learning	From Scratch	Semi-supervised MoCo	Semi-Supervised Autoencoder	Semi-supervised PCLR	Transfer Learning	From Scratch	Semi-supervised MoCo
200	N/A	N/A	N/A	N/A	N/A	0.997(0.452)	0.864(0.224)	0.881(0.287)	1.435(0.654)	0.796(0.157)
500	N/A	N/A	N/A	N/A	N/A	1.005(0.393)	0.907(0.096)	1.031(0.356)	1.163(0.293)	0.824(0.057)
1000	N/A	N/A	N/A	N/A	N/A	1.01(0.223)	0.86(0.106)	1.017(0.34)	1.18(0.337)	0.793(0.059)
2000	1.215(1.235)	0.673(0.281)	1.251(1.168)	2.272(2.169)	0.648(0.263)	1.204(0.267)	0.877(0.095)	1.073(0.18)	1.217(0.216)	0.802(0.049)
5000	1.802(1.776)	0.701(0.15)	1.093(0.666)	1.874(0.635)	0.76(0.177)	1.161(0.211)	0.905(0.095)	1.143(0.175)	1.212(0.157)	0.841(0.068)
10000	1.506(0.848)	0.713(0.122)	1.127(0.455)	1.722(0.475)	0.7(0.096)	1.268(0.314)	0.935(0.048)	1.22(0.176)	1.278(0.122)	0.874(0.05)
20000	1.332(0.571)	0.717(0.126)	0.977(0.266)	1.555(0.297)	0.785(0.087)	1.372(0.169)	0.963(0.032)	1.19(0.11)	1.186(0.082)	0.872(0.035)
40000	1.113(0.076)	0.716(0.014)	1.055(0.038)	1.684(0.215)	0.806(0.005)	1.275(0.003)	0.973(0.002)	1.238(0.007)	1.099(0.051)	0.868(0.001)

Appendix Table D.3: Calibration of semi-supervised and supervised models in the NLST dataset. Results are not available for some smaller training sets due to insufficient events.

PLCO	One-year death			Twelve-Year Death		
	Self-supervised Autoencoder	Self-Supervised PCLR	Self-Supervised MoCo	Self-Supervised Autoencoder	Self-Supervised PCLR	Self-Supervised MoCo
200	N/A	N/A	N/A	1.032(0.206)	1.024(0.206)	1.027(0.202)
500	N/A	N/A	N/A	1.048(0.084)	1.052(0.079)	1.052(0.08)
1000	N/A	N/A	N/A	1.006(0.069)	1.003(0.066)	1.003(0.067)
2000	1.209(0.249)	1.114(0.412)	1.112(0.413)	1.02(0.057)	1.017(0.055)	1.014(0.058)
5000	1.135(0.119)	1.201(0.249)	1.202(0.247)	1.024(0.033)	1.021(0.033)	1.019(0.032)
10000	1.227(0.087)	1.136(0.116)	1.133(0.119)	1.033(0.017)	1.031(0.018)	1.028(0.017)
20000	1.218(0.231)	1.221(0.086)	1.219(0.085)	1.035(0.016)	1.033(0.017)	1.031(0.015)
40000	1.204(0.002)	1.206(0.0)	1.201(0.001)	1.034(0.0)	1.031(0.0)	1.031(0.0)

Appendix Table D.4: Calibration of Self-Supervised models in the PLCO dataset

NLST	One-year death			Twelve-Year Death		
	Self-Supervised Autoencoder	Self-Supervised PCLR	Self-Supervised MoCo	Self-Supervised Autoencoder	Self-Supervised PCLR	Self-Supervised MoCo
200	N/A	N/A	N/A	1.361(1.167)	0.864(0.224)	0.778(0.17)
500	N/A	N/A	N/A	0.831(0.196)	0.907(0.096)	0.806(0.062)
1000	N/A	N/A	N/A	1.2(0.894)	0.86(0.106)	0.781(0.06)
2000	0.935(0.611)	0.673(0.281)	0.638(0.205)	1.104(0.68)	0.877(0.095)	0.794(0.062)
5000	0.965(0.783)	0.701(0.15)	0.712(0.147)	0.566(0.314)	0.905(0.095)	0.784(0.033)
10000	0.958(0.592)	0.713(0.122)	0.675(0.07)	0.389(0.142)	0.935(0.048)	0.805(0.025)
20000	1.196(0.649)	0.717(0.126)	0.723(0.052)	0.379(0.068)	0.963(0.032)	0.826(0.021)
40000	1.004(0.002)	0.716(0.014)	0.711(0.005)	0.388(0.006)	0.973(0.002)	0.831(0.001)

Appendix Table D.5: Calibration of self-supervised models in the NLST dataset.

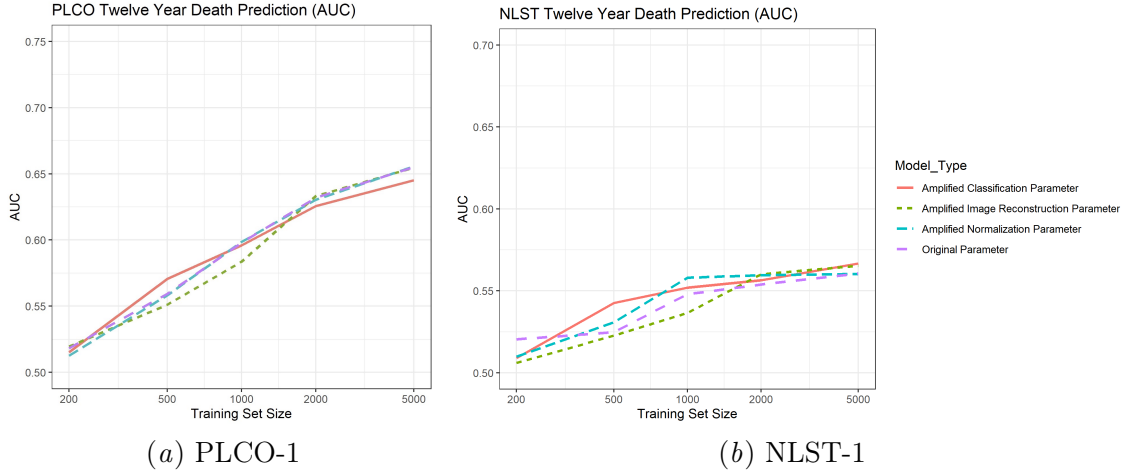
## Appendix E. Hyperparameter Sensitivity Analysis

We performed a sensitivity analysis on the hyperparameters for the Autoencoder-Classifier's loss function  $\lambda_{reg}, \lambda_{recon}, \lambda_{norm}$ . The default parameters were  $(1, 20, 0.0001)$ . We tested the following configurations:

- Amplified Classification & Regression parameter  $\lambda_{reg}$ :  $(10, 20, 0.0001)$
- Amplified Image reconstruction parameter  $\lambda_{recon}$ :  $(1, 200, 0.0001)$
- Amplified Normalization parameter  $\lambda_{norm}$ :  $(1, 20, 0.001)$

Using each parameter setting, we trained separate models on a randomly selected set of 7000 radiographs from the pretraining datasets and tested them on PLCO and NLST to predict 12-year mortality: [Figure E.9](#) and [Table D.1](#).

The results for different hyperparameters are generally consistent with each other. However, amplification of the classification loss shows a slight disadvantage for internal validation when the training set size is large, and a slight advantage for both internal and external validation when the training set size is small. It is possible that a larger discrepancy may emerge if a larger subset of images is used for training. Currently, scaling up any of the hyperparameters does not significantly impact the AUC showing the robustness of the approach.



Appendix Figure E.9: AUC comparisons for 12-year mortality rate between different hyperparameter settings.

## Appendix F. Prediction of intermediate risk factors

		PLCO Internal Validation			
	Target Variable	Semi-Supervised Autoencoder	Semi-Supervised MoCo	Semi-Supervised PCLR	Transfer Learning
Continuous Demographics and Risk Factors	Age	0.654 (0.64,0.66)	0.465 (0.45,0.48)	0.392 (0.38,0.41)	0.373 (0.36,0.39)
	BMI	0.823 (0.82,0.83)	0.629 (0.62,0.64)	0.732 (0.72,0.74)	0.656 (0.65,0.67)
	Pack-Years	0.332 (0.31,0.35)	0.205 (0.18,0.23)	0.217 (0.2,0.24)	0.202 (0.18,0.22)
Discrete Demographics and Risk Factors	Black Race	0.947 (0.94,0.95)	0.776 (0.76,0.79)	0.845 (0.83,0.86)	0.794 (0.78,0.81)
	History of Type 2 Diabetes	0.752 (0.74,0.77)	0.669 (0.65,0.69)	0.709 (0.69,0.72)	0.667 (0.65,0.68)
	History of Emphysema	0.799 (0.77,0.82)	0.677 (0.65,0.7)	0.676 (0.65,0.7)	0.684 (0.66,0.71)
	History of Smoking	0.675 (0.67,0.68)	0.622 (0.61,0.63)	0.63 (0.62,0.64)	0.622 (0.61,0.63)
	History of Myocardial Infarction	0.763 (0.75,0.78)	0.673 (0.66,0.69)	0.7 (0.68,0.72)	0.662 (0.65,0.68)
	Hispanic Ethnicity	0.789 (0.76,0.82)	0.728 (0.7,0.76)	0.746 (0.72,0.78)	0.684 (0.65,0.72)
	History of Hypertension	0.696 (0.69,0.7)	0.644 (0.63,0.65)	0.661 (0.65,0.67)	0.649 (0.64,0.66)
	History of Osteoporosis	0.804 (0.79,0.82)	0.76 (0.74,0.78)	0.745 (0.73,0.76)	0.708 (0.69,0.73)
	History of Cancer	0.649 (0.63,0.67)	0.619 (0.6,0.64)	0.629 (0.61,0.65)	0.602 (0.58,0.62)
	Sex	0.999 (1,1)	0.991 (0.99,0.99)	0.987 (0.99,0.99)	0.958 (0.96,0.96)
Radiologist Findings	History of Stroke	0.672 (0.64,0.7)	0.602 (0.57,0.63)	0.62 (0.59,0.65)	0.593 (0.56,0.62)
	Atelectasis	0.753 (0.56,0.95)	0.523 (0.26,0.78)	0.628 (0.43,0.83)	0.576 (0.29,0.86)
	Bone/Chest Wall Lesion	0.761 (0.74,0.78)	0.694 (0.67,0.72)	0.731 (0.71,0.75)	0.665 (0.64,0.69)
	Cardiovascular Abnormality	0.89 (0.88,0.9)	0.786 (0.77,0.81)	0.811 (0.79,0.83)	0.81 (0.79,0.83)
	COPD/Emphysema	0.842 (0.82,0.86)	0.752 (0.73,0.78)	0.785 (0.76,0.81)	0.745 (0.72,0.77)
	Lung Fibrosis	0.704 (0.69,0.72)	0.608 (0.59,0.62)	0.612 (0.6,0.63)	0.629 (0.61,0.65)
	Lung Opacity	0.68 (0.63,0.73)	0.569 (0.52,0.62)	0.562 (0.51,0.61)	0.586 (0.53,0.64)
	Lymphadenopathy	0.725 (0.67,0.78)	0.67 (0.62,0.72)	0.59 (0.52,0.66)	0.563 (0.5,0.63)
	Lung Nodule	0.617 (0.6,0.63)	0.59 (0.57,0.61)	0.593 (0.57,0.61)	0.559 (0.54,0.58)
	Pleural Fibrosis	0.723 (0.7,0.75)	0.646 (0.62,0.67)	0.633 (0.61,0.66)	0.613 (0.59,0.64)

Appendix Table F.6: Comparison of prediction of intermediate risk factors for supervised and semi-supervised models on the PLCO dataset using Pearson Correlation for continuous variables and AUC for discrete variables. Results indicate superior performance of the semi-supervised autoencoder in most target tasks.

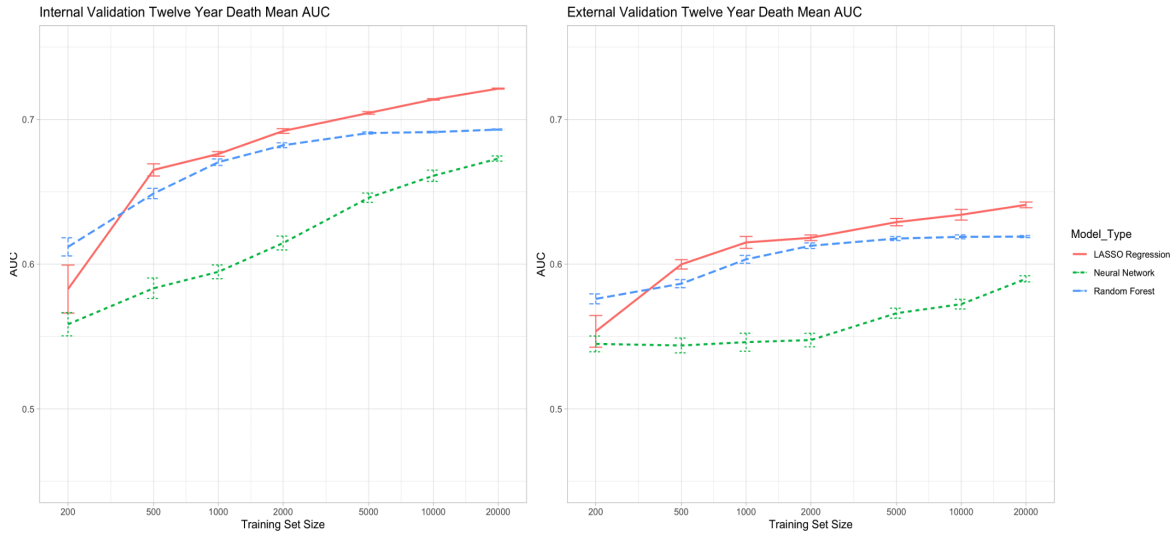
		NLST External Validation				
		Target Variable	Semi-Supervised Autoencoder	Semi-Supervised MoCo	Semi-Supervised PCLR	Transfer Learning
Continuous Demographics and Risk Factors	Age	0.547 (0.53,0.57)	0.465 (0.44,0.49)	0.226 (0.2,0.25)	0.407 (0.38,0.43)	
	BMI	0.761 (0.75,0.77)	0.493 (0.47,0.51)	0.63 (0.61,0.65)	0.68 (0.67,0.69)	
	Pack-Years	0.181 (0.16,0.21)	0.166 (0.14,0.19)	0.101 (0.07,0.13)	0.156 (0.13,0.18)	
Discrete Demographics and Risk Factors	History of Type 2 Diabetes	0.737 (0.72,0.76)	0.651 (0.63,0.68)	0.679 (0.66,0.7)	0.704 (0.68,0.73)	
	History of Emphysema	0.609 (0.58,0.64)	0.574 (0.54,0.6)	0.573 (0.54,0.6)	0.637 (0.61,0.67)	
	History of Myocardial Infarction	0.669 (0.65,0.69)	0.625 (0.6,0.65)	0.622 (0.6,0.64)	0.657 (0.63,0.68)	
	History of Hypertension	0.634 (0.62,0.65)	0.595 (0.58,0.61)	0.608 (0.59,0.62)	0.644 (0.63,0.66)	
	History of Cancer	0.637 (0.6,0.68)	0.602 (0.56,0.64)	0.543 (0.51,0.58)	0.576 (0.54,0.61)	
	Sex	0.993 (0.99,1)	0.974 (0.97,0.98)	0.905 (0.9,0.91)	0.917 (0.91,0.92)	
	History of Stroke	0.596 (0.55,0.64)	0.528 (0.48,0.57)	0.578 (0.53,0.62)	0.601 (0.56,0.64)	
Radiologist Findings	Atelectasis	0.611 (0.53,0.69)	0.501 (0.41,0.59)	0.566 (0.47,0.66)	0.588 (0.5,0.67)	
	Bone/Chest Wall Lesion	0.608 (0.54,0.68)	0.511 (0.43,0.59)	0.569 (0.49,0.64)	0.507 (0.43,0.58)	
	Cardiovascular Abnormality	0.721 (0.67,0.77)	0.77 (0.73,0.81)	0.715 (0.67,0.76)	0.808 (0.76,0.85)	
	COPD/Emphysema	0.638 (0.62,0.66)	0.6 (0.58,0.62)	0.643 (0.63,0.66)	0.679 (0.66,0.69)	
	Lung Fibrosis	0.606 (0.58,0.63)	0.572 (0.55,0.59)	0.51 (0.49,0.53)	0.542 (0.52,0.56)	
	Lung Opacity	0.65 (0.55,0.75)	0.539 (0.43,0.65)	0.496 (0.4,0.59)	0.534 (0.41,0.65)	
	Lymphadenopathy	0.615 (0.53,0.7)	0.521 (0.44,0.6)	0.615 (0.54,0.69)	0.526 (0.44,0.61)	
	Lung Nodule	0.544 (0.53,0.56)	0.521 (0.5,0.54)	0.527 (0.51,0.54)	0.541 (0.52,0.56)	
	Pleural Fibrosis	0.514 (0.49,0.54)	0.558 (0.53,0.58)	0.499 (0.47,0.52)	0.598 (0.57,0.62)	

Appendix Table F.7: Prediction accuracy of intermediate risk factors using supervised and semi-supervised models on the NLST external validation dataset. We observed similar findings as in the internal validation (PLCO) results.

		PLCO Internal Validation			NLST External Validation			
		Target Variable	Self-Supervised PCLR	Self-Supervised Autoencoder	Self-Supervised MoCo	Self-Supervised PCLR	Self-Supervised Autoencoder	Self-Supervised MoCo
Continuous Demographics and Risk Factors	Age	0.469 (0.46,0.48)	0.433 (0.42,0.45)	0.196 (0.18,0.21)	0.368 (0.34,0.39)	0.126 (0.1,0.15)	0.121 (0.09,0.15)	
	BMI	0.744 (0.74,0.75)	0.73 (0.72,0.74)	0.509 (0.5,0.52)	0.692 (0.68,0.71)	0.464 (0.44,0.48)	0.349 (0.33,0.37)	
	Pack-Years	0.246 (0.22,0.27)	0.226 (0.21,0.25)	0.171 (0.15,0.19)	0.153 (0.13,0.18)	0.044 (0.02,0.07)	0.083 (0.06,0.11)	
Discrete Demographics and Risk Factors	History of Type 2 Diabetes	0.715 (0.7,0.73)	0.689 (0.67,0.7)	0.635 (0.62,0.65)	0.705 (0.68,0.73)	0.558 (0.53,0.59)	0.58 (0.55,0.61)	
	History of Emphysema	0.709 (0.68,0.74)	0.672 (0.64,0.7)	0.64 (0.61,0.67)	0.617 (0.59,0.65)	0.542 (0.51,0.57)	0.567 (0.54,0.6)	
	History of Smoking	0.641 (0.63,0.65)	0.629 (0.62,0.64)	0.615 (0.61,0.62)	NA	NA	NA	
	History of Myocardial Infarction	0.712 (0.7,0.73)	0.689 (0.67,0.7)	0.631 (0.62,0.65)	0.652 (0.63,0.67)	0.546 (0.52,0.57)	0.571 (0.55,0.59)	
	History of Hypertension	0.675 (0.67,0.68)	0.667 (0.66,0.68)	0.606 (0.6,0.62)	0.629 (0.61,0.64)	0.559 (0.54,0.57)	0.564 (0.55,0.58)	
	History of Osteoporosis	0.762 (0.75,0.78)	0.747 (0.73,0.76)	0.721 (0.7,0.74)	NA	NA	NA	
	History of Cancer	0.633 (0.61,0.66)	0.616 (0.59,0.64)	0.631 (0.61,0.65)	0.563 (0.52,0.6)	0.537 (0.5,0.58)	0.503 (0.47,0.54)	
	Sex	0.992 (0.99,0.99)	0.982 (0.98,0.98)	0.943 (0.94,0.95)	0.949 (0.94,0.95)	0.754 (0.74,0.77)	0.728 (0.71,0.74)	
	History of Stroke	0.626 (0.59,0.66)	0.585 (0.55,0.62)	0.532 (0.5,0.57)	0.551 (0.51,0.59)	0.504 (0.46,0.55)	0.511 (0.47,0.56)	
	Atelectasis	0.556 (0.29,0.82)	0.613 (0.47,0.76)	0.54 (0.4,0.68)	0.548 (0.46,0.63)	0.548 (0.47,0.63)	0.551 (0.46,0.64)	
Radiologist Findings	Bone/Chest Wall Lesion	0.727 (0.7,0.75)	0.704 (0.68,0.73)	0.689 (0.67,0.71)	0.569 (0.5,0.64)	0.615 (0.54,0.69)	0.499 (0.42,0.57)	
	Cardiovascular Abnormality	0.841 (0.82,0.86)	0.79 (0.77,0.81)	0.736 (0.71,0.76)	0.809 (0.77,0.85)	0.628 (0.57,0.68)	0.639 (0.59,0.69)	
	COPD/Emphysema	0.783 (0.76,0.81)	0.775 (0.75,0.8)	0.697 (0.67,0.72)	0.65 (0.63,0.67)	0.597 (0.58,0.61)	0.567 (0.55,0.59)	
	Lung Fibrosis	0.647 (0.63,0.66)	0.603 (0.59,0.62)	0.564 (0.55,0.58)	0.6 (0.58,0.62)	0.503 (0.48,0.53)	0.512 (0.49,0.54)	
	Lung Opacity	0.607 (0.55,0.66)	0.541 (0.49,0.59)	0.556 (0.5,0.61)	0.533 (0.45,0.62)	0.538 (0.45,0.63)	0.497 (0.42,0.58)	
	Lymphadenopathy	0.671 (0.61,0.73)	0.634 (0.58,0.69)	0.58 (0.52,0.64)	0.566 (0.48,0.65)	0.505 (0.41,0.6)	0.565 (0.49,0.64)	
	Lung Nodule	0.59 (0.57,0.61)	0.576 (0.56,0.59)	0.572 (0.55,0.59)	0.542 (0.52,0.56)	0.524 (0.51,0.54)	0.513 (0.5,0.53)	
	Pleural Fibrosis	0.66 (0.63,0.69)	0.624 (0.6,0.65)	0.607 (0.58,0.63)	0.58 (0.55,0.61)	0.509 (0.48,0.53)	0.519 (0.49,0.55)	

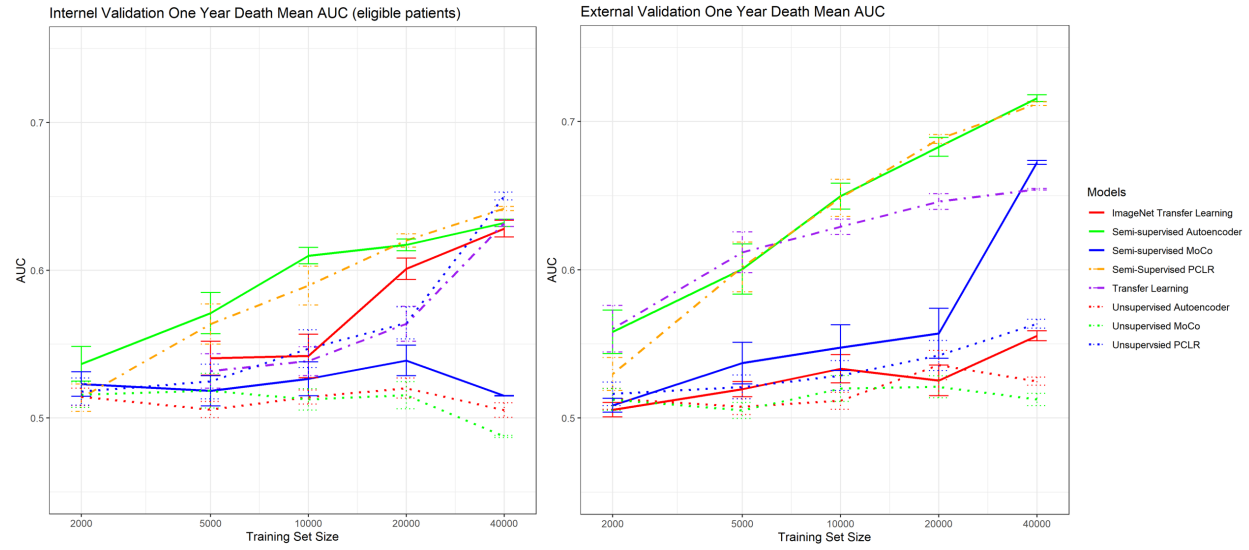
Appendix Table F.8: Prediction accuracy of intermediate risk factors using self-supervised models on PLCO (internal validation) and NLST (external validation). Results indicate superior performance of Self-Supervised Contrastive Learning and Autoencoder in most tasks.

## Appendix G. A Comparison of Results of Different Downstream Task Models

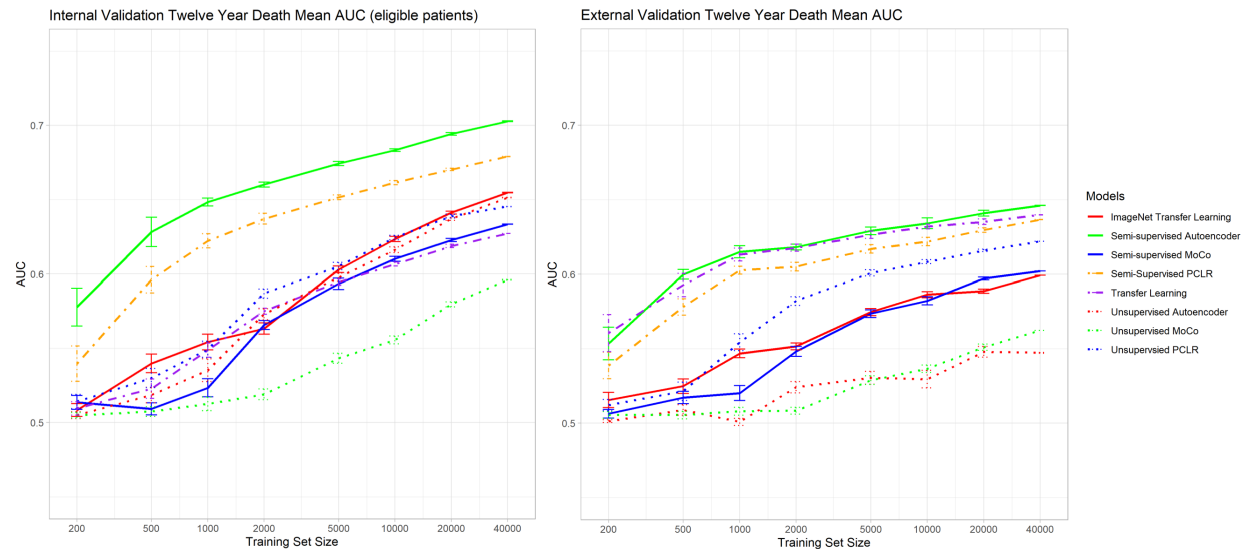


Appendix Figure G.10: The performance of LASSO regression, a neural network with one hidden layer and nonlinear activation, and a random forest with 10 max nodes and 10 trees were evaluated using AUC on 12-year mortality rate prediction with the PLCO dataset. Results showed that LASSO had the best AUC performance across all training sizes. However, the neural network failed to converge in most trials of size 40,000, therefore trial size 40,000 was not included in the final analysis.

## Appendix H. Effect of cohort differences on validation set performance



Appendix Figure H.11: Left: PLCO internal validation results (only participants meeting NLST entry criteria), Right: NLST external validation results.



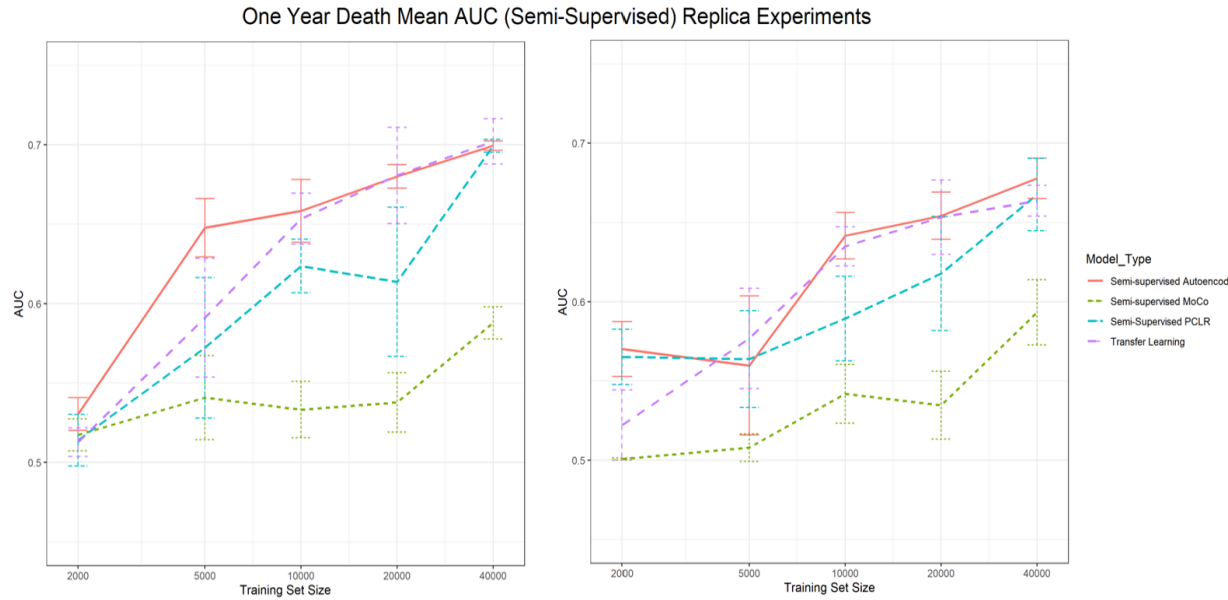
Appendix Figure H.12: Left: PLCO internal validation results (only participants meeting NLST entry criteria), Right: NLST external validation results.

## Appendix I. Cohort Characteristics

	Pretraining	Training	Testing		
	CheXpert	NIH-CXR14	PLCO Training	PLCO Internal Testing	NLST External Testing
Description	All adults with posterior-anterior chest x-rays from Stanford University Hospital between October 2002 and July 2017.	All adults with posterior-anterior chest x-rays from the NIH Clinical Center between 1992 and 2015.	Adults in the chest x-ray arm of the Prostate, Lung, Colorectal, and Ovarian cancer screening trial. Adults 55-74 years from 21 US sites.	Testing set individuals from PLCO trial.	Adults in the chest x-ray arm of the National Lung Screening Trial. Heavy cigarette smokers 55-74 years with no history of lung cancer from 10 US sites
Demographics					
Age	57.0 (17.2)	48.8 (14.8)	62.4 (5.4)	62.4 (5.4)	61.7 (5.0)
Female Sex	10134 / 29419 (34.4%)	28965 / 64628 (44.8%)	18073 / 37467 (48.2%)	6631 / 13723 (48.3%)	2416 / 5414 (44.6%)
Race					
White	NA	NA	32524 / 37433 (86.7%)	11915 / 13708 (86.9%)	5088 / 5389 (55.9%)
Black	NA	NA	2194 / 37433 (5.9%)	807 / 13708 (5.9%)	208 / 5389 (3.9%)
Other	NA	NA	2010 / 37433 (5.4%)	732 / 13708 (5.3%)	93 / 5389 (1.7%)
Radiology Findings					
No Finding	9589 / 29419 (32.6%)	37452 / 64628 (58.0%)	NA	NA	NA
Pleural Effusion	8078 / 29419 (27.5%)	6450 / 64628 (10.0%)	NA	NA	NA
Lung Opacity	9736 / 29419 (33.1%)	NA	292 / 37467 (0.8%)	111 / 13723 (0.8%)	33 / 5414 (0.6%)
Lung Lesion	2122 / 29419 (7.2%)	6972 / 64628 (10.8%)	2892 / 37467 (7.7%)	971 / 13723 (7.1%)	1610 / 5414 (29.7%)
Infiltration	NA	8976 / 64628 (13.9%)	NA	NA	NA
Atelectasis	3195 / 29419 (10.9%)	5614 / 64628 (8.7%)	20 / 37467 (0.0%)	6 / 13723 (0.0%)	43 / 5414 (0.8%)
Pneumothorax	1802 / 29419 (6.1%)	3268 / 64628 (5.1%)	NA	NA	NA
Cardiac Abnormality	NA	NA	1496 / 37467 (4.0%)	536 / 13723 (3.9%)	122 / 5414 (2.3%)
Cardiomegaly	2909 / 29419 (9.9%)	1520 / 64628 (2.4%)	NA	NA	NA
Consolidation	1498 / 29419 (5.1%)	1463 / 64628 (2.3%)	NA	NA	NA
Pleural Thickening	NA	2366 / 64628 (3.7%)	NA	NA	NA
Edema	1709 / 29419 (5.8%)	268 / 64628 (0.4%)	NA	NA	NA
Pneumonia	1198 / 29419 (4.1%)	586 / 64628 (0.9%)	NA	NA	NA
Emphysema	NA	1473 / 64628 (2.3%)	974 / 37467 (2.6%)	371 / 13723 (2.7%)	1197 / 5414 (22.1%)
Enlarged Cardiomediastinum	1436 / 29419 (4.9%)	NA	NA	NA	
Fracture	1411 / 29419 (4.8%)	NA	NA	NA	
Lung Fibrosis	NA	1394 / 64628 (2.2%)	2858 / 37467 (7.6%)	1059 / 13723 (7.7%)	700 / 5414 (12.9%)
Other Pleural Findings	1012 / 29419 (3.4%)	NA	1184 / 37467 (3.2%)	416 / 13723 (3.0%)	471 / 5414 (8.7%)
Hernia	NA	191 / 64628 (0.3%)	NA	NA	NA
Bone/ Chest Wall Lesion	NA	NA	1663 / 37467 (4.4%)	596 / 13723 (4.3%)	61 / 5414 (1.1%)
Lymphadenopathy	NA	NA	230 / 37467 (0.6%)	71 / 13723 (0.5%)	46 / 5414 (0.8%)
Risk Factors					
BMI	NA	NA	27.3 (4.9)	27.3 (4.9)	27.8 (5.3)
Pack-Years	NA	NA	35.2 (28.8)	35.6 (29.6)	55.7 (23.5)
History of Type 2 Diabetes	NA	NA	2864 / 37410 (7.7%)	1046 / 13694 (7.6%)	501 / 5402 (9.3%)
History of Emphysema	NA	NA	861 / 37399 (2.3%)	335 / 13697 (2.4%)	642 / 5414 (11.9%)
History of MI	NA	NA	3255 / 37405 (8.7%)	1207 / 13692 (8.8%)	665 / 5391 (12.3%)
History of Hypertension	NA	NA	12432 / 37414 (33.2%)	4633 / 13700 (33.8%)	1985 / 5399 (36.8%)
History of Cancer	NA	NA	1632 / 37453 (4.4%)	576 / 13716 (4.2%)	225 / 5414 (4.2%)
History of Stroke	NA	NA	845 / 37407 (2.3%)	308 / 13697 (2.2%)	173 / 5392 (3.2%)
Outcomes					
1-year mortality	NA	NA	153 / 37467 (0.5%)	48 / 13723 (0.3%)	33 / 5414 (0.6%)
12-year mortality	NA	NA	4983 / 37467 (13.3%)	1800 / 13723 (13.1%)	931 / 5414 (17.2%)

Appendix Table I.9: Cohort Characteristics

## Appendix J. Effect of random weight initialization

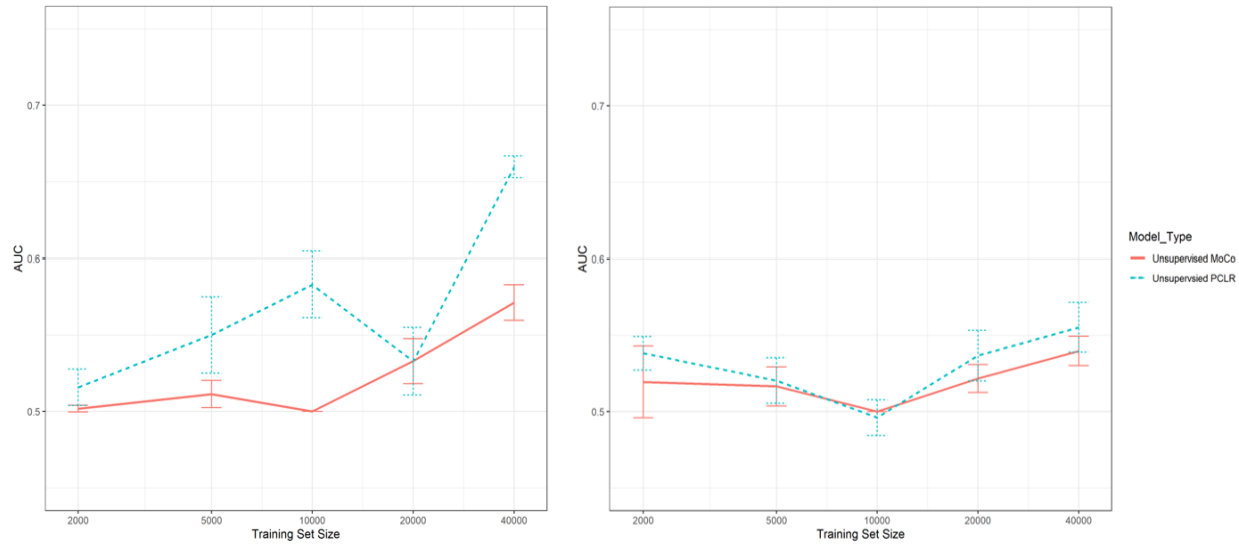


Appendix Figure J.13: Left: internal validation (PLCO), Right: external validation (NLST).



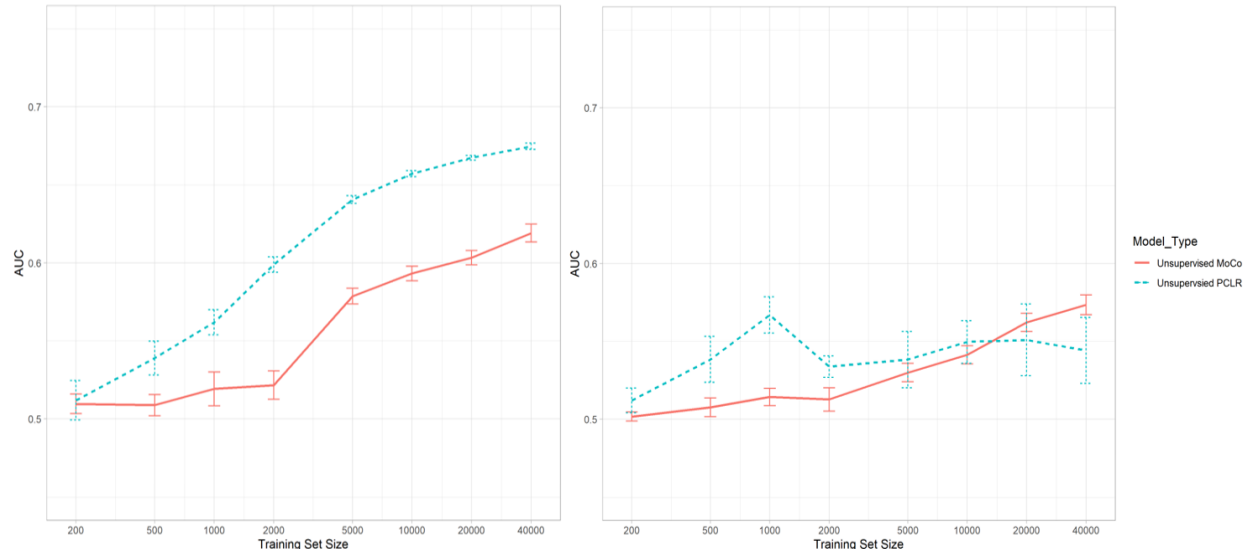
Appendix Figure J.14: Left: internal validation (PLCO), Right: external validation (NLST).

## One Year Death Mean AUC (Semi-Supervised) Replica Experiments



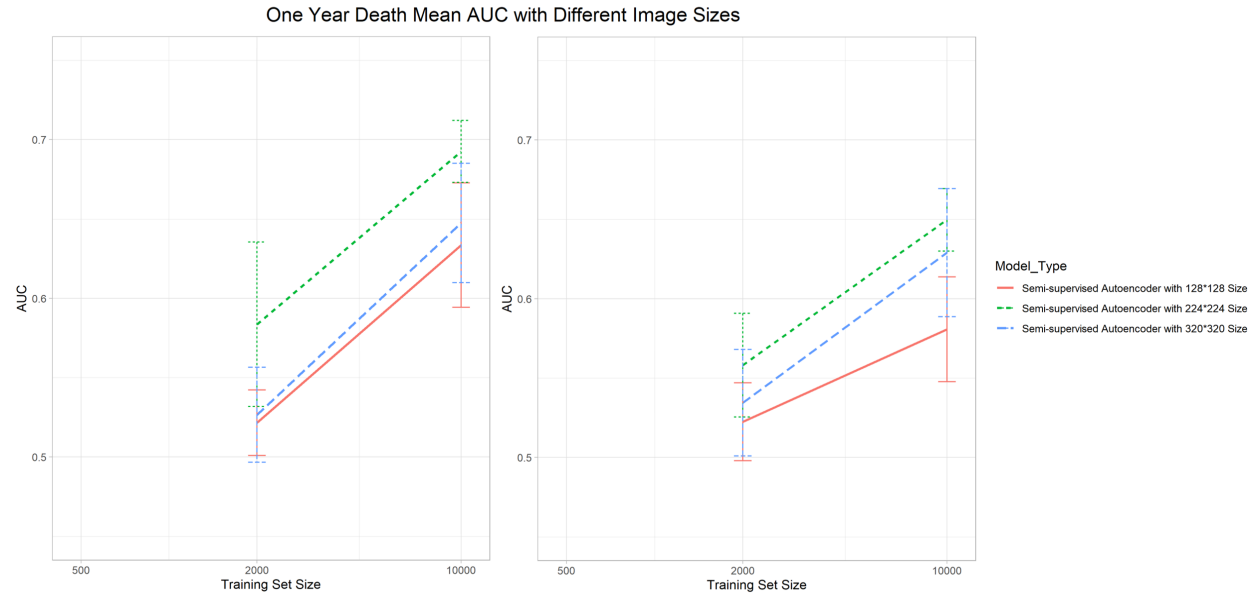
Appendix Figure J.15: Left: internal validation (PLCO), Right: external validation (NLST).

## Twelve Year Death Mean AUC (Self-Supervised) Replica Experiments

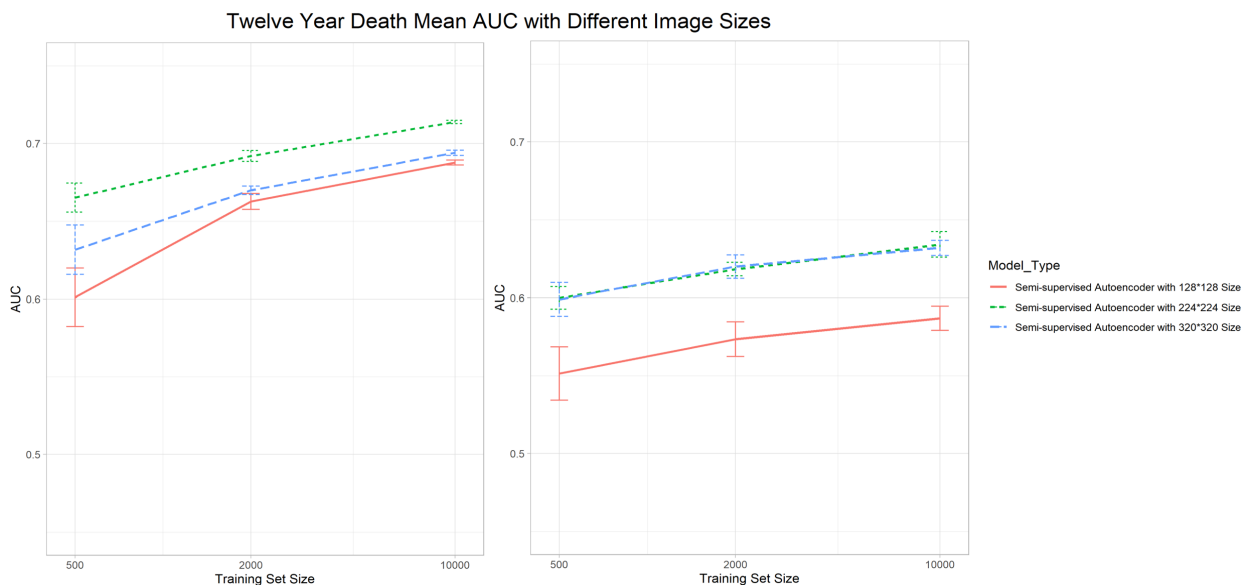


Appendix Figure J.16: Left: internal validation (PLCO), Right: external validation (NLST).

## Appendix K. Effect of Image resolution



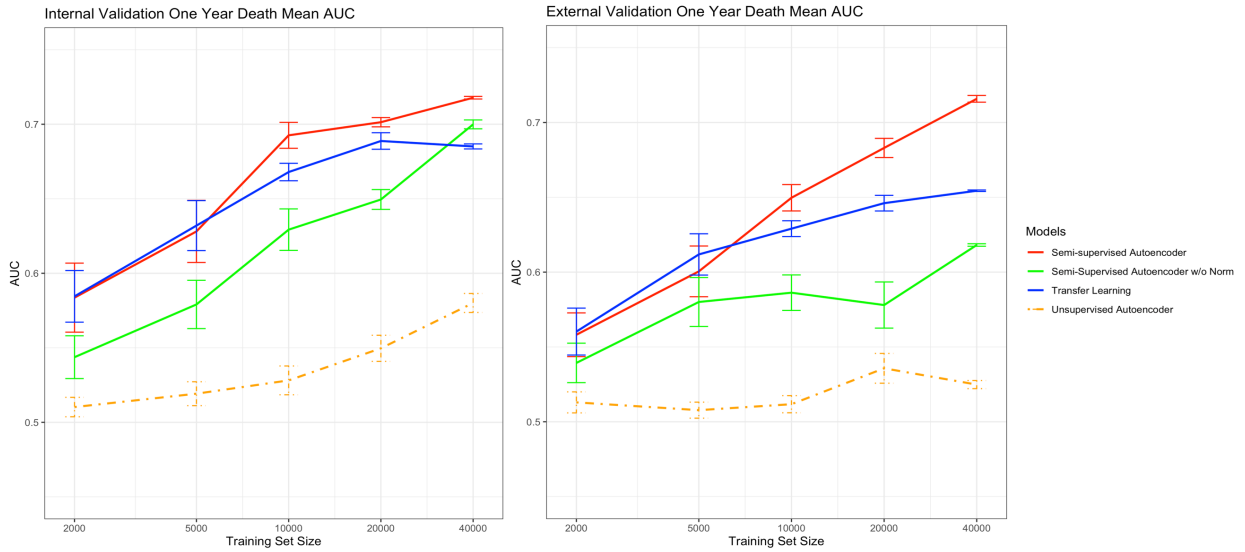
Appendix Figure K.17: Left: internal validation (PLCO), Right: external validation (NLST). Pre-training models were trained using 128\*128, 224\*224 (original semi-supervised autoencoder model), and 320\*320 as pre-training image sizes. All other procedures, including encodings extraction and experiments, are held the same.



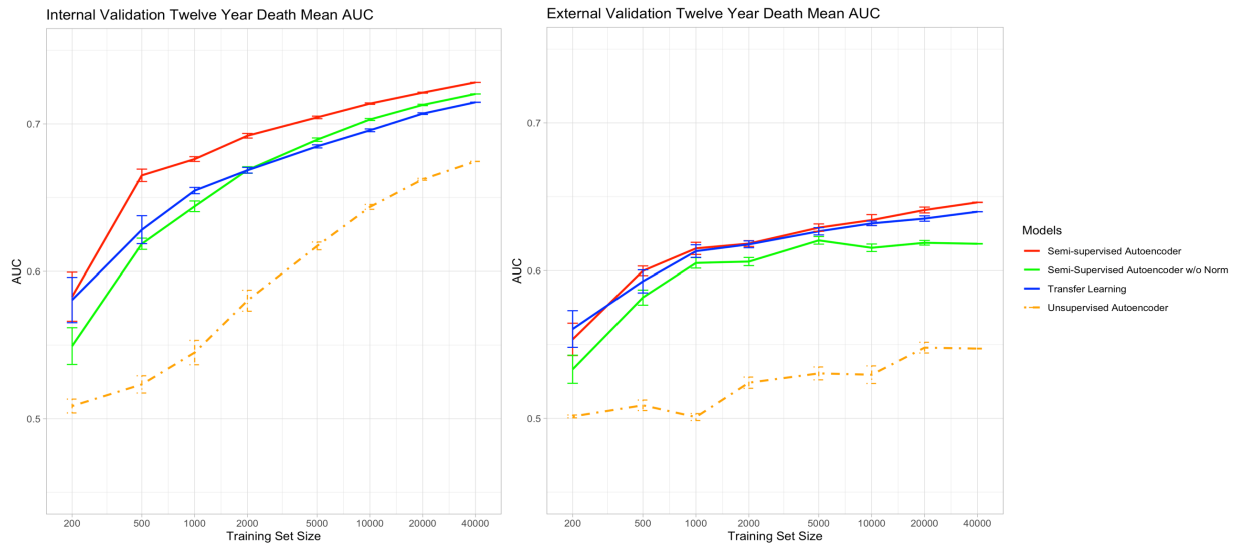
Appendix Figure K.18: Left: internal validation (PLCO), Right: external validation (NLST). Pre-training models were trained using 128\*128, 224\*224 (original semi-supervised autoencoder model), and 320\*320 as pre-training image sizes. All other procedures, including encodings extraction and experiments, are held the same.

## Appendix L. Autoencoder Ablation Experiments

Here, we show an ablation experiment to show the impact of each component of the semi-supervised autoencoder model. Our major finding is that semi-supervision contributes the most to performance; however, the self-supervision adds additional value for rare outcomes (1-year mortality).



Appendix Figure L.19: Left: PLCO internal validation results, Right: NLST external validation results.



Appendix Figure L.20: Left: PLCO internal validation results, Right: NLST external validation results.

